Montanuniversität Leoben

Influence of Ta on the thermal stability of $Ti_{1-x}Al_xN$ hard coatings deposited with different bias voltages

Diploma Thesis

by

Andreas Jamnig

This work has been carried out at the Chair of Functional Materials and Material Systems,
Montanuniversität Leoben, Austria.

Leoben, June 2016

Financial support by the Austrian Federal Government (in particular from Bundesministerium für Verkehr, Innovation und Technologie and Bundesministerium für Wirtschaft, Familie und Jugend) represented by Österreichische Forschungsförderungsgesellschaft mbH (project number 845255) is gratefully acknowledged.

Affidavit

I declare in lieu of oath, that I wrote this thesis and performed the associated research myself, using only literature cited in this volume

Leoben, June 2016

Acknowledgements

My sincerest gratitude to Univ.-Prof. Dipl.-Ing. Dr. Christian Mitterer, head of the Chair of Functional Materials and Material Systems, for the opportunity to write this thesis at his chair. *Thank you for also being interested in my future plans and supporting them!*

I am very grateful to my supervisor Dipl.-Ing. Birgit Großmann, for her valuable advice during the research and writing of this thesis. *Thank you for your patience and letting me annoy you with questions whenever I needed to!*

I would like to express my gratitude to Dipl.-Ing. Dr. Nina Schalk, for the supervision and thorough read-through of this thesis. *Thank you for adding precision to this work by asking the right questions!*

I am thankful to Dipl.-Ing. Markus Pohler and Dipl.-Ing. Dr. Christoph Czettl from Ceratizit Austria, for providing the coatings for this thesis and helping during the determination of the mechanical properties.

Furthermore, I would like to thank the entire Thin Film Group, for the nice chats during coffee and lunch breaks, interesting discussions and helping whenever I needed it. *Thank you all for letting me become a part of your group in such a short time!*

A special thanks goes to the dear friends I found during my time in Leoben. You were: Motivating me to learn more and finish my studies. Sitting behind me while writing this thesis and making me feel bad whenever I did “internet research”. Having “one” beer with me, no matter the time, place or circumstances. *You know who you are, thank you!*

Finally, I want to thank my family, my parents, siblings, grandmothers, aunts and uncles, for their love and support in my decisions. *Mama, Papa, danke für die finanzielle Unterstützung über so viele Jahre und euer Vertrauen in mich! Ohne euch hätte ich diesen Abschluss nie geschafft!*

Table of contents

1 Introduction

High production rates are a substantial element to ensure economically competitive manufacturing processes. In the machining industry, cutting processes can be a limiting factor because cutting tools are subject to high tribological, thermal and mechanical loads. Consequently, the implementation of higher cutting speeds and thus production rates demands cutting tools with higher high-temperature hardness, strength and wear resistance on the one hand and elasticity and toughness on the other hand. As this combination of properties cannot be found in conventional materials, composites of tough or ductile substrates and thin hard and wear resistant coatings are commonly used [1].

TiN coatings deposited by vapor deposition techniques have been used for many years for cutting applications due to their high hardness and melting point, enabling them to withstand tribological demands [2]. However, these coatings start to oxidize at low temperatures compared to the temperatures they are exposed to during cutting applications [3, 4]. Thus it has been proposed to further alloy TiN with Al [5, 6], which results in enhanced oxidation resistance and mechanical properties. Furthermore, age hardening of the ternary $Ti_{1-x}Al_xN$ system leads to a hardness increase at elevated temperatures [7]. In the last decade, the effect of a fourth alloying element on the decomposition of the system has been studied and Ta is one of the most promising candidates [8, 9].

In the present thesis, the effect of an increasing Ta content on microstructure, mechanical properties and thermal stability of a $Ti_{1-x}Al_xN$ coating system with a Ti/Al atomic ratio of 50/50 deposited by cathodic arc evaporation was investigated. The as-deposited coatings and coatings after annealing in a vacuum furnace were evaluated using X-ray diffraction (XRD) and nanoindentation. Additionally, differential scanning calorimetry (DSC) was performed on powdered coatings to detect microstructural changes during the heating process. Furthermore, the influence of three different bias voltages on the microstructure and the mechanical properties was studied for selected coatings.

2 Deposition of hard coatings

Hard coatings are deposited on components used for applications where wear and corrosion resistance are of importance. Amongst others these include consumables in the cutting industry, e.g. turning or milling inserts or drills, elements in the automotive industry, e.g. combustion liners, or the foundry industry, e.g. molds and dies [1].

Several techniques are utilized to deposit hard coatings on a material, which is typically called substrate in the coating industry. However, they vary considerably in properties that can be obtained for individual coatings, deposition rates and temperatures [10]. Vapor deposition techniques are widely used for the deposition of hard coatings and include three steps: (*i*) Creation of a vapor phase, (*ii*) transport of the vapor particles to the substrate and (*iii*) condensation of the particles and formation of a dense coating. In general, two types of vapor deposition techniques can be distinguished: Chemical vapor deposition (CVD) and physical vapor deposition (PVD) [11].

2.1 Chemical vapor deposition

During CVD, gaseous chemical reactants are introduced into a reaction chamber. There, they are activated thermally (conventional or thermal CVD), by a plasma (plasma assisted CVD) or laser (laser induced CVD). A vapor is formed through a chemical reaction of the reactants, such as oxidation, reduction or pyrolysis, and condenses on the substrate. Although a wide range of coatings can be synthesized with CVD, its drawback is that only substrates that withstand high temperatures (> 900 °C) can be coated and that the three deposition steps are interdependent [1, 10, 11].

2.2 Physical vapor deposition

In the course of PVD, a solid material is evaporated through physical effects. Using PVD, the substrate temperature can be regulated in a wide range, thus also temperature sensitive substrates can be coated. PVD techniques can be further subdivided, depending on the way the vapor is created. However, two methods are predominantly used to deposit hard coatings, namely sputter deposition and cathodic arc evaporation (CAE).

During sputter deposition, ions of a gaseous material are accelerated towards a solid, called target, in an electric field. There, target atoms are ejected due to energy and momentum transfer from the bombarding ions. This process is called physical sputtering. The particles originating from the target, which are mainly neutrals, are then transported to and deposited on a substrate. Compounds can be deposited by sputtering a compound target or by sputtering an elemental target in the presence of a reactive gas, called reactive sputtering [12].

For CAE, a high current low voltage arc vaporizes an electrode, creating a highly ionized vapor (up to 100 %) that is accelerated towards a biased substrate. An arc is a self-sustained discharge between a cathode and an anode, capable of supporting large currents by providing its own mechanism of electron emission. The term “cathodic arc” stresses out that the arc forms at the cathode. It can form in a vacuum or gaseous atmosphere, therefore, the terms “vacuum arc” and “gaseous arc” are used, respectively. However, it is clear that the discharge cannot be sustained in a vacuum, due to a lack of chargeable particles. The term “vacuum arc” rather emphasizes that the arc is ignited (e.g. by a mechanical igniter) in a volume containing a vacuum prior to the ignition. Conducting particles origin from the cathode itself and include electrons and multiply charged ions, which are emitted from the arc spot, i.e. the point of contact between arc and cathode. The atmosphere “gaseous arcs” are formed in can contain reactive gases, which can be used to create compound coatings. Arcs are driven to prominent positions on the cathode surface, generated by the roughness every technical surface has, and very high current densities (10^9 - 10^{10} A/m^2) form locally. Thus the cathode is subject to heating, resulting in thermal evaporation of particles [12].

One negative effect during CAE is the ejection of macro particles, which are formed by emission of molten target material. They are incorporated into the growing films, where they act as defects, deteriorating the mechanical properties and film adhesion. Therefore, different means are used to filter the macro particles, for example a plasma duct that deflects the plasma while not influencing the macro particles [12, 13]. An advantage of CAE in comparison to other deposition techniques is the high ionization rate of target atoms and formation of multiply charged ions. By applying a negative so called bias voltage to the substrate holder and consequently, by changing the potential of the substrate with respect to the plasma potential, these particles are accelerated more strongly towards the substrate. Hence, impinging particles have a high energy, which is introduced to the system, facilitating diffusion and resulting in a high coating density. Altering the bias voltage leads to a change of the deposition rate and energy of impinging particles and therefore to a change in the morphology of the growing coating. Consequently, the stress state of the coating is also influenced. Residual stress in the deposited coating strongly affects the coating's properties, e.g. hardness, elastic modulus and adhesion. Tensile residual stresses are unfavorable as they promote crack formation and growth [11, 13]. All coatings investigated within the present thesis were deposited via CAE.

2.3 Morphology of thin films

2.3.1 Nucleation and growth

During deposition, vaporized particles impact on the substrate surface with different energies, determining whether they are reflected immediately or adsorbed, forming adatoms [11]. In the course of the following condensation phase the adatoms diffuse on the surface. If the interactions between two adatoms are stronger than the interaction between adatom and surface, they form clusters. However, if the adatom-surface interaction is stronger, they condensate on surface discontinuities as illustrated in Figure 2.1. The former nucleation type is called "island-" or Volmer-Weber mode, the latter "layer-by-layer-" or Frank-Van der Merwe mode. Another nucleation type, which is also shown in Figure 2.2 is the "layer and island-" or Stranski-Krastanov mode, where monolayers are formed in early stages of film growth and islands form on top of them [14].

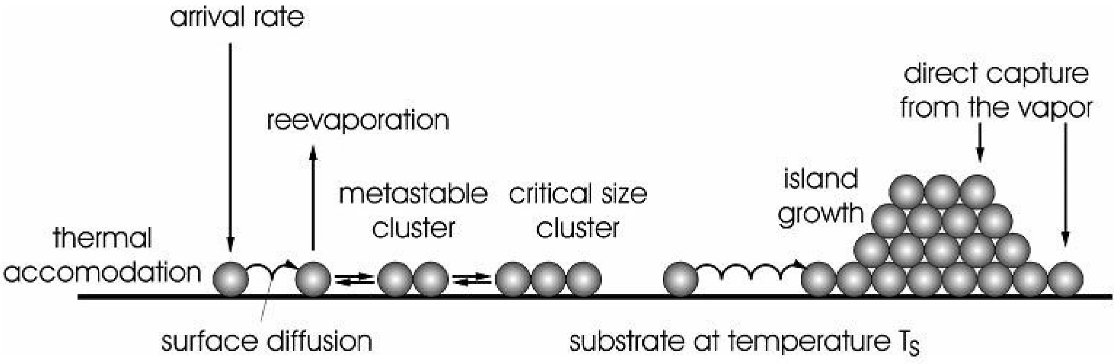

Figure 2.1: Schematic of the processes leading to nucleation and film growth [15].

Once the clusters reach a critical size they start to grow, incorporating smaller clusters in the capture zone around them and arriving particles, until the clusters touch and coalesce, minimizing their surface energy and exposing additional substrate surface. New clusters can then form on these surfaces during secondary nucleation, closing channels and holes, which are not covered during primary nucleation, creating a continuous film [14].

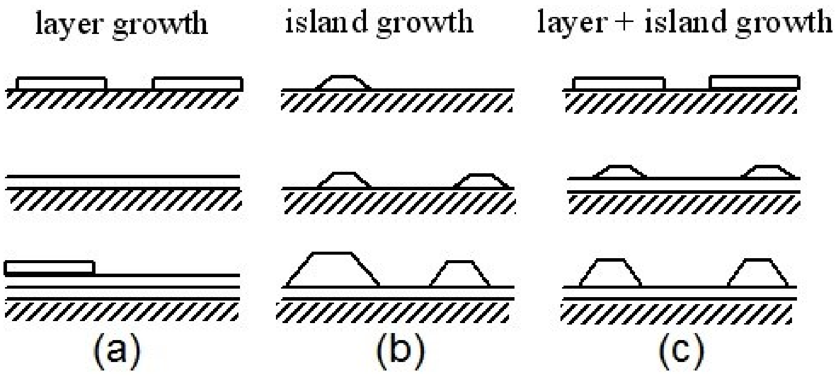

Figure 2.2: Schematic of thin film growth modes: (a) layer growth, (b) island growth and (c) mixed layer-island growth [15].

2.3.2 Structure zone diagram

The deposition and growth of films depend on many different parameters, making it complicated to illustrate which parameter affects the film growth in which way. Therefore structure zone diagrams (SZDs) have been developed, limiting the number of influencing parameters to a few important. Due to these simplifications, SZDs cannot be expected to describe the exact microstructure of a film for given deposition parameters, but rather are guidelines to possible microstructures. The SZD proposed by Anders is shown in Figure 2.3 [16]. It illustrates the expected microstructure, texture and film thickness t* of a coating in dependence of the generalized homologous temperature *T** and the energy E* of arriving particles. *T** is defined as

$$T^* = T_h + T_{pot}, \tag{2.1}$$

where T_h is the homologous temperature, the ratio of film temperature and melting temperature, and T_{pot} takes the temperature shift due to the potential energy of arriving particles into account. Particles, that are accelerated towards the surface by a bias voltage, have a high kinetic energy when arriving at the substrate and therefore cause displacement of surface atoms and heating, which is represented by the energy E* on the second axis. The z-axis describes the net thickness t* of the film.

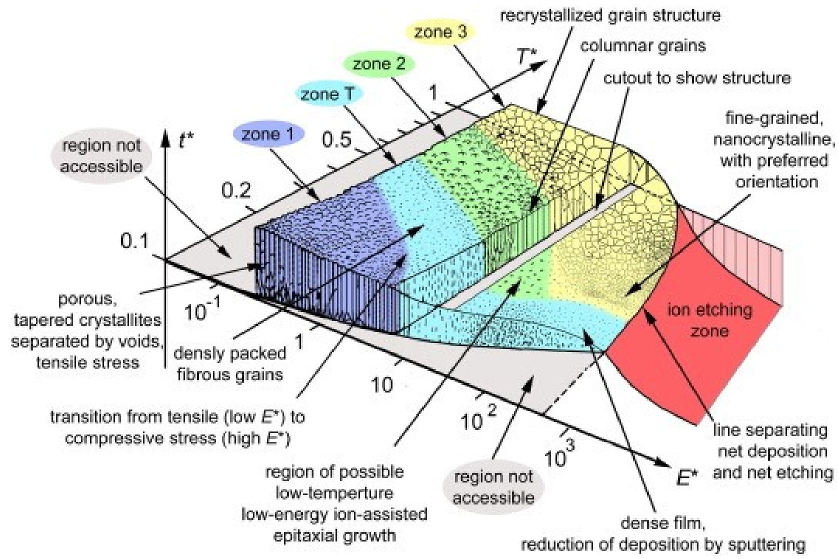

Figure 2.3: Structure zone diagram proposed by Anders [16].

Within the SZD, four different zones can be distinguished, three of which described by Movchan and Demchishin (zones 1, 2 and 3) [17], and the fourth by Thornton (zone T) [18]. Three basic processes can be correlated with the formation of the zones: (*i*) shadowing, the interaction of the surface roughness with the angle of incidence of arriving coating atoms, (*ii*) surface diffusion and (*iii*) bulk diffusion. Porous, tapered crystals dominate the microstructure of zone 1, which is formed at $T^* < 0.4$ and low E^*. The low T^* results in a high number of defects in the microstructure and voids at the grain boundaries due to impeded diffusion and shadowing effects. Zone T is a transition area between the zones 1 and 2 at $0.4 < T^* < 0.6$. It contains fibrous grains with dense grain boundaries due to beginning surface diffusion. The range of zone T increases with higher E^* towards lower T^* because surface diffusion is promoted by the energy of the impinging atoms. Surface diffusion becomes the dominating process for $0.6 < T^* < 0.8$ and allows the growth of columnar grains in zone 2, with a low defect density and distinct grain boundaries. For even higher T^*, bulk diffusion is possible and equiaxed grains that reach through the whole film thickness can form in zone 3.

3 Thermally induced processes

3.1 General

Coatings synthesized by PVD techniques can exhibit phase compositions far from the thermodynamic equilibrium and microstructures with a high number of internal defects. These defects can be categorized according to their complexity [19]: zero dimensional point defects (interstitial atoms, vacancies), one dimensional line defects (dislocations), two dimensional area defects (grain boundaries, phase boundaries) and three dimensional volume defects (pores, precipitations). Adding defects to a perfect crystal increases the system's total energy, which also increases the driving force for diffusion.

Diffusion is the movement of atoms or ions due to concentration gradients and is described by Fick's first law

$$j_D = -D\nabla c, \tag{3.1}$$

where j_D is the diffusion current, D is the diffusion coefficient and c the concentration of the diffusing element. The diffusion rate is strongly related to the state of the matter, being considerably higher in gases and liquids compared to solids. Due to their crystal structure, metals and ceramics have a very strong interaction of neighboring atoms. Therefore, the activation energy for diffusion, which strongly depends on atomic interactions, is higher for solids. Defects can weaken these interactions, leading to a decrease of the activation energy and therefore promoted diffusion. Diffusion kinetics also depends strongly on whether the diffusing particle is solved substitutionally or interstitially in the lattice. Latter is preferred by atoms considerably smaller than the lattice constant and leads to an overall higher diffusivity [19].

Overcoming the activation energy becomes significantly easier at elevated temperatures, since that leads to a higher energy of the diffusing particles on the one hand and to a decreasing bonding energy within the crystal on the other hand. Latter can be explained by a more narrow interatomic potential. Therefore some processes, such as recovery and recrystallization, can only take place at elevated temperatures [19].

3.2 Recovery

The first process that can be observed when heating a crystalline material is recovery, a process dominated by defect annihilation and rearrangement of defect positions. Due to the elevated temperatures, interstitials and vacancies are able to recombine or form voids as illustrated in Figure 3.1. The driving force for recovery is the reduction of microstrain, stemming from microstructural defects in the crystal. There are three types of residual stresses that foster microstrain: (*i*) Residual stresses of first order are far-reaching and affect a larger number of grains. (*ii*) Residual stresses of second order are homogeneous in one crystallite, while (*iii*) residual stresses of third order are inhomogeneous and change within atomic distances [20].

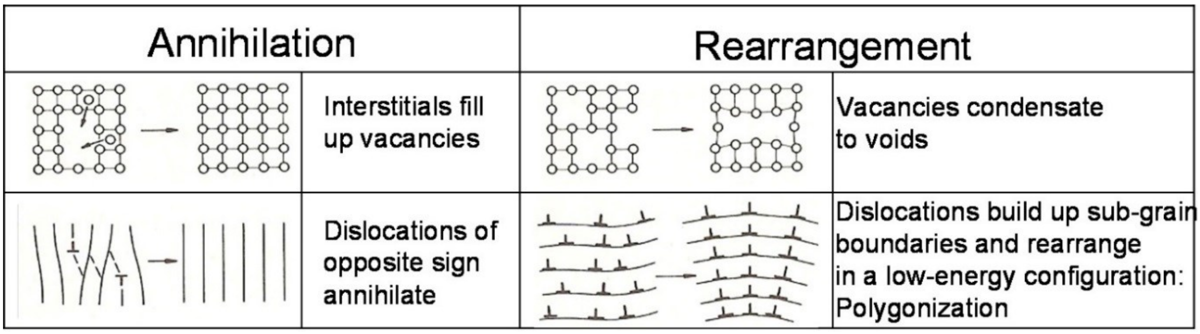

Figure 3.1: Overview of recovery processes in metals redrawn from [19, 21].

Two basic types of dislocations have to be considered during recovery: *(i)* Screw-dislocations, which have no preferred glide plane and are therefore able to cross-glide at low temperatures, when coming into contact with repulsive stress fields. *(ii)* Edge-dislocations have one preferred glide plane and cannot leave it at low temperatures. However, at elevated temperatures diffusion of vacancies and interstitials enables dislocations to climb and leave their preferred glide plane. During recovery processes, dislocations are thus able to recombine or rearrange themselves, minimizing the stored energy and forming sub-grain boundaries. These effects lead to a decrease of the defect density and consequently to a deterioration of mechanical properties such as elastic modulus and hardness. Particles retard diffusion of dislocations in the crystal, and consequently recovery, as they are obstacles the dislocations have to overcome [19, 20].

3.3 Recrystallization

The driving force for recrystallization is the reduction of the energy stored in defects, lowering the overall energy of the system in the process. Its kinetics can be described by

$$f = 1 - \exp(-kt^n), \tag{3.2}$$

the Johnson-Mehl-Avrami-Kolmogorov equation, where f is the volume fraction of the recrystallized phase, k depends on the nucleation and growth rates and n is a numerical exponent, which is independent of temperature, if the nucleation mechanism does not change. Recrystallization is governed by nucleation and grain growth, both being related to diffusion, and thus temperature. Areas with high defect densities, such as grain boundaries or the sub-grain boundaries formed during recovery, act as sites for initial nucleation. Grain growth rates are influenced by the mobility of (sub-)grain boundaries and their ability for gliding and climbing. Coalescence of neighboring grains is another crucial aspect of recrystallization and can include rotation of sub-grains as depicted in Figure 3.2 [19, 20].

As shown before, recrystallization can occur at elevated temperatures and once primary recrystallization is finished, a material exhibits a microstructure with few defects and uniform grain size. However, if the temperature remains high, further grain growth can be observed, driven by the minimization of the grains' surface energy. This leads to the growth of big grains at the cost of smaller ones and single, very coarse grains can form. This stage of recrystallization is also called abnormal grain growth, leading to less uniform mechanical properties and thus often to an inferior performance of the material [20].

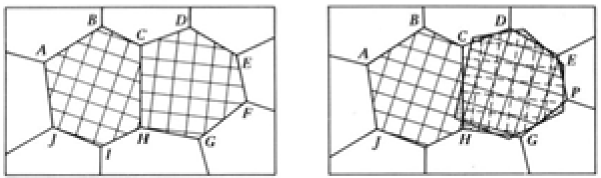

(a)
Original subgrain structure before coalescence

(b)
One subgrain is undergoing a rotation

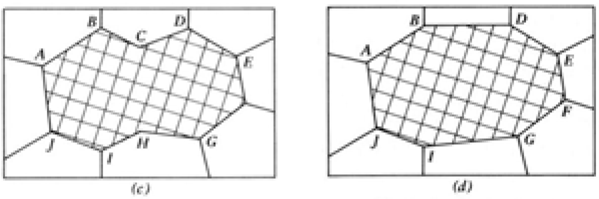

(c)
Subgrain structure just after coalescence

(d)
Final subgrain structure after some subboundary migration

Figure 3.2: Schematic of the coalescence of sub-grains with indicated lattice orientations (a) before, (b) during, (c) shortly after and (d) after the coalescence [20].

3.4 Decomposition

The free enthalpy G of a system, or rather its minimization, determines which phases are stable and which microstructure can possibly form. The following considerations are valid for a binary system (A, B) with the composition X showing a miscibility gap, which is quenched from the higher temperature T_1 to a lower temperature T_2. Figure 3.3a shows the corresponding phase diagram. For binary systems which satisfy the condition

$$H_{AB} > \frac{H_{AA} + H_{BB}}{2}, \tag{3.3}$$

where H_{ij} is the binding enthalpy of the neighboring atoms i and j (i = A, B, j = A, B), G develops two minima as illustrated in Figure 3.3b and decomposition can occur. Depending on the composition of the system, decomposition takes place via nucleation and growth or spontaneously without incubation time, also called spinodal decomposition [22].

An alloy with the composition X_0 has a high free enthalpy G_0, however, the G-X curve has a negative curvature at this composition. Therefore, small fluctuations in the composition lead to a decrease in G, making the system unstable and decompose. Contrary to what is usually expected from diffusion, the fraction of B increases in areas with already high B concentrations as shown in Figure 3.3d, which is why it is also called “up-hill” diffusion. The areas where G has a negative curvature are called the spinodal. The G-X curve for alloys with compositions outside the spinodal (e.g. X_0') has a positive curvature. Therefore, concentration fluctuations lead to an increase of G and are energetically unfavorable. Hence, nuclei with very different compositions from the matrix have to form (X_1, X_2), which consequently can grow as depicted in Figure 3.3c. The stable phases forming through these two decomposition pathways are the same, but the microstructure which is formed via nucleation and growth can be expected to be coarser [19, 22].

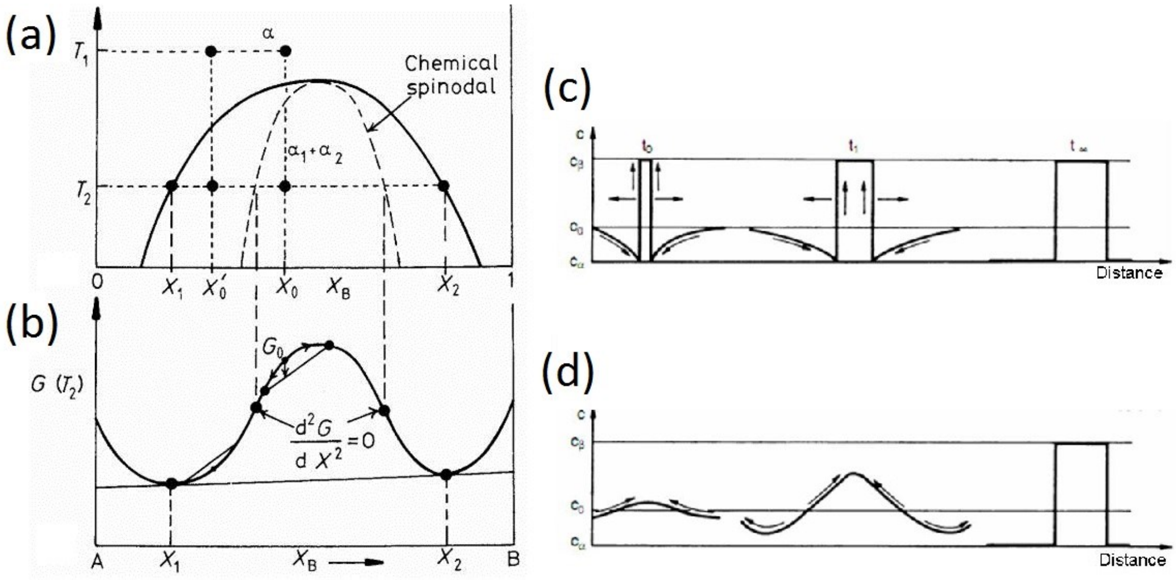

Figure 3.3: (a) Phase diagram and (b) free entropy G of a binary system with a miscibility gap [22]. Evolution of concentrations during (c) decomposition via nucleation and growth and (d) spinodal decomposition [19].

4 Titanium aluminum nitride

4.1 Microstructure

AlN, forming a wurtzite (w-) crystal structure, is almost insoluble in the cubic (c-) TiN crystal as shown in Figure 4.1a. Therefore, PVD techniques are used to synthesize thermodynamically unstable $Ti_{1-x}Al_xN$ supersaturated solid solutions. They can form because conditions during PVD are often far from the thermodynamic equilibrium [23]. These metastable solid solutions can be described with the quasi-binary phase diagram shown in Figure 4.1b. The $Ti_{1-x}Al_xN$ solid solutions exhibit a cubic structure up to x ~ 0.65, where the smaller Al atoms substitute for Ti atoms, leading to a decrease of the lattice constant. For higher AlN contents the wurtzite structure is more stable, which is illustrated in Figure 4.1c [24–26].

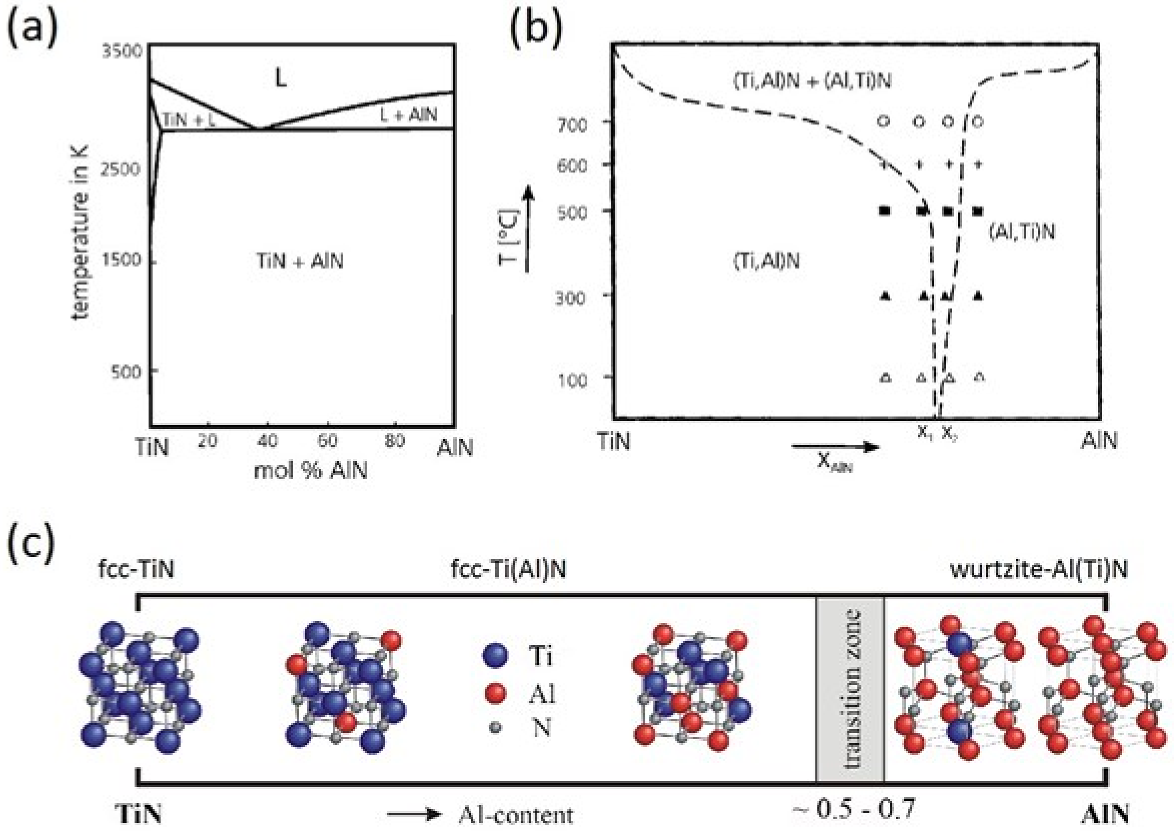

Figure 4.1: (a) Stable phase diagram [24] and (b) the modified metastable phase diagram [25] of the quasi-binary system TiN/AlN. (c) Evolution of the microstructure of the ternary system $Ti_{1-x}Al_xN$ with increasing AlN content [26].

According to solid solution hardening, the hardness of materials within the cubic system increases with higher Al contents until the wurtzite structure starts to form, leading to a hardness decrease which is shown in Figure 4.2. Thus, maximum hardness can be obtained for solid solutions with the highest Al content at which the cubic structure can be maintained [27].

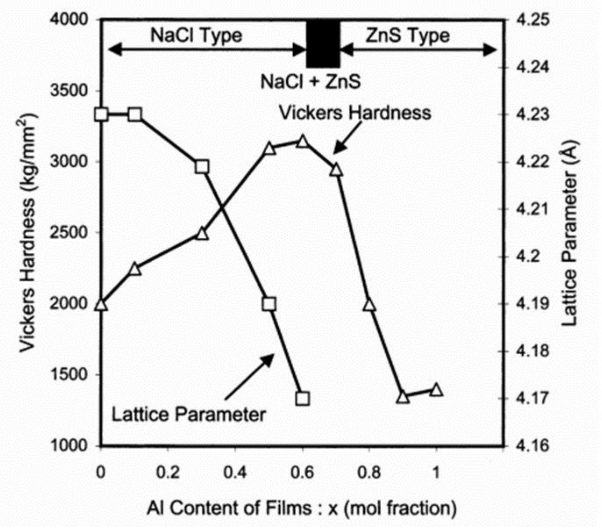

Figure 4.2: Decrease of the lattice parameter and consequent increase of the hardness of the ternary $Ti_{1-x}Al_xN$ system with increasing AlN content. At higher AlN contents wurtzite (ZnS) AlN forms and the hardness decreases considerably [7].

4.2 Thermal stability

In air TiN starts to oxidize at temperatures above 550 °C, forming porous rutile- and anatase-type TiO_2 [3, 4]. Alloying of Al to the TiN system results in an enhanced wear behavior and improved oxidation resistance. In the ternary $Ti_{1-x}Al_xN$ system, a dense and protective Al_2O_3 rich top layer is formed at temperatures higher than 700 °C [28]. A rutile-type TiO_2 intermediate layer is formed between this top layer and the $Ti_{1-x}Al_xN$ coating [29, 30].

Additionally to the hardness increase at room temperature (RT) and the improved oxidation resistance, the alloying with Al induces age hardening effects due to spinodal decomposition. During decomposition, c-TiN rich domains and c-AlN rich domains are formed which is illustrated in Figure 4.3 [27, 31, 32]. The formation of these domains leads to an increase of elastic and plastic properties of the system due to the formation of coherency strains [33]. The c-AlN transforms into the stable wurtzite structure at temperatures higher than 900 °C, resulting in a deterioration of the mechanical and tribological properties of the protective coatings which is not favorable during application [2, 27]. Consequently, a significant research topic in the last decade has been the stabilization of the cubic phase by alloying.

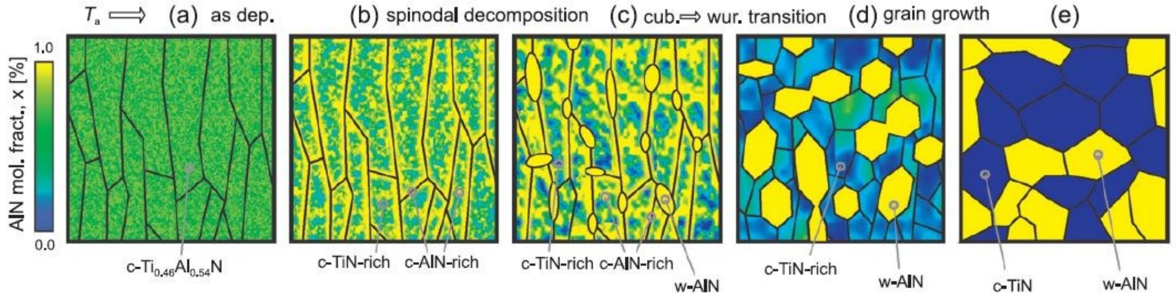

Figure 4.3: Schematic representation of the structural evolution of a cubic (c-) $Ti_{1-x}Al_xN$ coating. (a) As-deposited state with small chemical fluctuations of the composition. (b) Formation of c-TiN and c-AlN rich domains via spinodal decomposition. (c) Ongoing decomposition and formation of wurtzite (w-) AlN. (d) Al diffusion out of the c-TiN grains and growth of w-AlN. (e) Grain growth of the dual phase structure [32].

4.3 Alloying with tantalum

Ta has been shown to improve the cutting performance of $Ti_{1-x}Al_xN$ for several reasons. On one hand the alloying leads to solid solution hardening [28]. Additionally, the incorporation of Ta in the $Ti_{1-x}Al_xN$ lattice does not decrease the solubility of Al in the cubic phase [34]. Holec *et al.* [9] showed that the mixing enthalpy of the $Ti_{1-y}Ta_yN$ system is negative, which is beneficial, since the addition of Ta decreases the mixing enthalpy for a constant Ti/Al ratio. As the positive mixing enthalpy of $Ti_{1-x}Al_xN$ is the driving force of spinodal decomposition, this leads to a higher thermal stability [9, 34].

Another positive effect is the higher oxidation resistance of $(Ti_{1-x}Al_x)_{1-y}Ta_yN$ compared to $Ti_{1-x}Al_xN$. During oxidation, Ta^{5+} substitutes for Ti^{4+} in the intermediate TiO_2 layer, reducing the number of oxygen vacancies and therefore limiting the diffusion of oxygen from the surface to the unoxidized coating [28, 35–37].

5 Experimental methods

5.1 Coating deposition

All coatings presented in this work were deposited at Ceratizit Austria GmbH in Reutte, Austria, utilizing an industrial scale Oerlikon Balzers Innova cathodic arc evaporation system with nitrogen as reactive gas. The targets used for the depositions were powder metallurgically produced. An overview of the target compositions and the correlating deposition parameters is given in Figure 5.1.

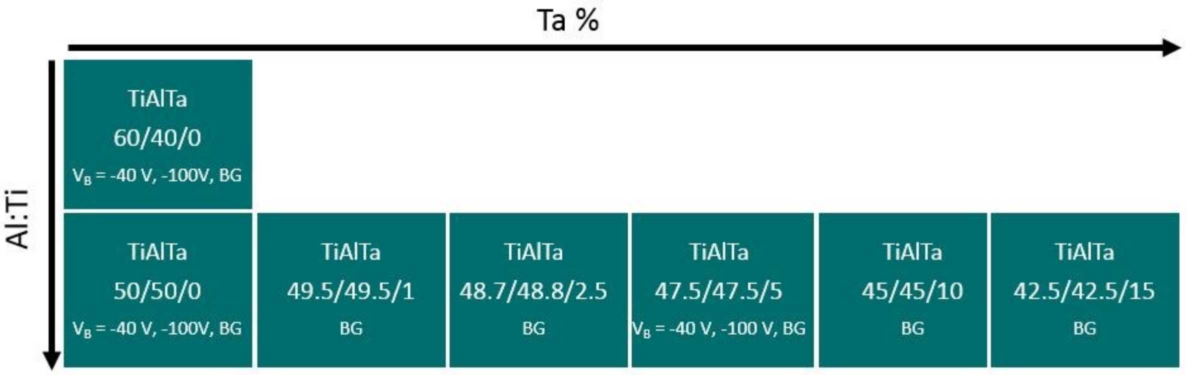

Figure 5.1: Overview of the used target compositions and deposition parameter sets with bias voltages V_B = -40 V, V_B = -100 V and a bias gradient (BG).

Three different sets of deposition parameters were used to investigate their influence on the coating properties. They differed mainly in the applied bias voltages (V_B), which remained at a constant level of -40 and -100 V for two sets, which will be hereinafter referred to as V_B = -40 V and V_B = -100 V, respectively. A change of the bias voltage from -40 V at the interface of substrate and coating to -70 V at the surface was used for the other set, henceforth called BG (= bias gradient). While the influence of the variation of the Ta content at a Ti/Al atomic ratio of 50/50 was investigated for coatings deposited with the BG parameter set, three target compositions ($Ti_{60}Al_{40}$, $Ti_{50}Al_{50}$ and $Ti_{47.5}Al_{47.5}Ta_5$) were selected to deposit coatings using all three parameter sets. The discussion of the $Ti_{0.6}Al_{0.4}N$ system can be found in the appendix.

Two different kinds of substrates were used. Coating properties were investigated on cemented carbide inserts (92 wt.% WC, 6 wt.% Co, 2 wt.% mixed carbide) with SNUN geometry (according to ISO 1832). The other substrate was a low alloy steel foil with a thickness of 50 µm. The coating deposited on this foil was used for powder preparation.

5.2 Powder preparation

Powders of the deposited coatings were prepared to allow DSC measurements, annealing tests and subsequent XRD measurements without influence of the substrate. Therefore, the low alloy steel substrate was dissolved in nitric acid (13 %mol), leaving differently sized flakes of the unaffected coating. These were then milled by hand in a porcelain mortar until a constant particle size was achieved.

5.3 Differential scanning calorimetry

Qualitative DSC measurements were conducted using a Setaram® LabSys Evo 2400 system to investigate at which temperatures thermally induced processes such as defect annihilation or decomposition occur in the $(Ti_{1-x}Al_x)_{1-y}Ta_yN$ system [38]. For each measurement, 20 ± 0.2 mg of powder were used in Al_2O_3 crucibles (volume: 100 µl), with an empty crucible as reference. The heat flow rates were recorded from RT up to 1500 °C with heating and cooling rates of 23 °C/min and 20 °C/min, respectively. Throughout the measurement, the system was purged with argon (gas flow: 200 mL/min) to prevent oxidation. The temperature-time profile was recorded twice consecutively, which allowed to annihilate the influence of reversible processes in the material by subtracting the heat flow rate recorded during the second heating step from one recorded during the first.

5.4 Annealing

The $(Ti_{1-x}Al_x)_{1-y}Ta_yN$ coatings and powders were annealed in a vacuum furnace (HTM Reetz, base pressure < $5x10^{-4}$ Pa) with subsequent XRD and nanoindentation measurements in order to assess thermally induced changes in microstructure and mechanical properties. Coated SNUN samples were annealed at temperatures between 700 and 1000 °C in steps of 50 °C. The holding time at maximum temperature was 15 min, the heating rate 20 °C/min and the cooling rate system dependent. Additionally, powder samples were annealed at 800, 980 and 1350 °C to determine the nature of the partial reactions observed in the DSC measurements.

5.5 X-ray diffraction

The analysis of the crystallographic structures of coatings and powders was performed utilizing a Bruker AXS D8 Advance X-ray diffractometer. Cu-K_α radiation with a wavelength $\lambda = 0.154$ nm was applied. The tube voltage was 40 kV and the tube current 40 mA. The samples were scanned from 32° to 47° with a step size of 0.02° and a step time of 1.2 s. Grazing incidence XRD with an incident angle of 2° was used for the coated samples to minimize the signal resulting from the substrate. For the powder the θ-2θ geometry was used.

The positions of the measured peaks and their corresponding crystal structures were determined using the DIFFRAC^{plus} EVA software provided by Bruker AXS and the implemented ICDD (International Centre for Diffraction Data) standards.

Furthermore, the lattice parameter a of the measured powders and coatings was calculated with a combination of Bragg's law and the plane-spacing equation for cubic crystals

$$a = \frac{\lambda}{2sin(\theta)}\sqrt{(h^2 + k^2 + l^2)}, \tag{5.1}$$

where λ is the wavelength of the utilized radiation, θ is the diffraction angle and (hkl) are the Miller indices that can be attributed to the measured peak [39].

5.6 Nanoindentation

Nanoindentation measurements were performed on coatings deposited on cemented carbide substrates with SNUN geometry. Prior to the measurement, the coating surface was polished with diamond suspensions (grain size 3 µm and 1 µm) to obtain a low and uniform surface roughness. A CSM Instruments Nanoindentation Tester with a Berkovich indenter was utilized. The maximum load was 30 mN, which was applied with a loading rate of 60 mN/min. To achieve reasonable statistics, 20 indents were performed on each sample.

6 Results and discussion

6.1 Alloying with tantalum

The influence of six different Ta contents on the $Ti_{1-x}Al_xN$ system with a constant Ti/Al atomic ratio of 50/50 was investigated using SNUN substrates in the as-deposited state. All samples were synthesized with the BG parameter set. XRD and nanoindentation measurements were conducted to determine changes in the microstructure and mechanical properties of the coatings with increasing Ta content. In addition, the evolution of microstructure and mechanical properties was investigated after annealing at temperatures between 700 and 1000 °C in steps of 50 °C. To gain a better understanding of the processes during annealing in the quaternary system, powders were prepared and qualitative DSC measurements conducted.

6.1.1 Microstructure

Figure 6.1 shows X-ray diffractograms for as-deposited $(Ti_{1-x}Al_x)_{1-y}Ta_yN$ coatings with Ta content increasing from bottom to top. The peaks originating from the $Ti_{0.5}Al_{0.5}N$ coating are located between the standard peak positions of c-TiN [40] and c-AlN [41], indicating that the coatings consists of a solid solution of these two components with a lattice constant corresponding to a Vegard-like behavior of the two phases [42].

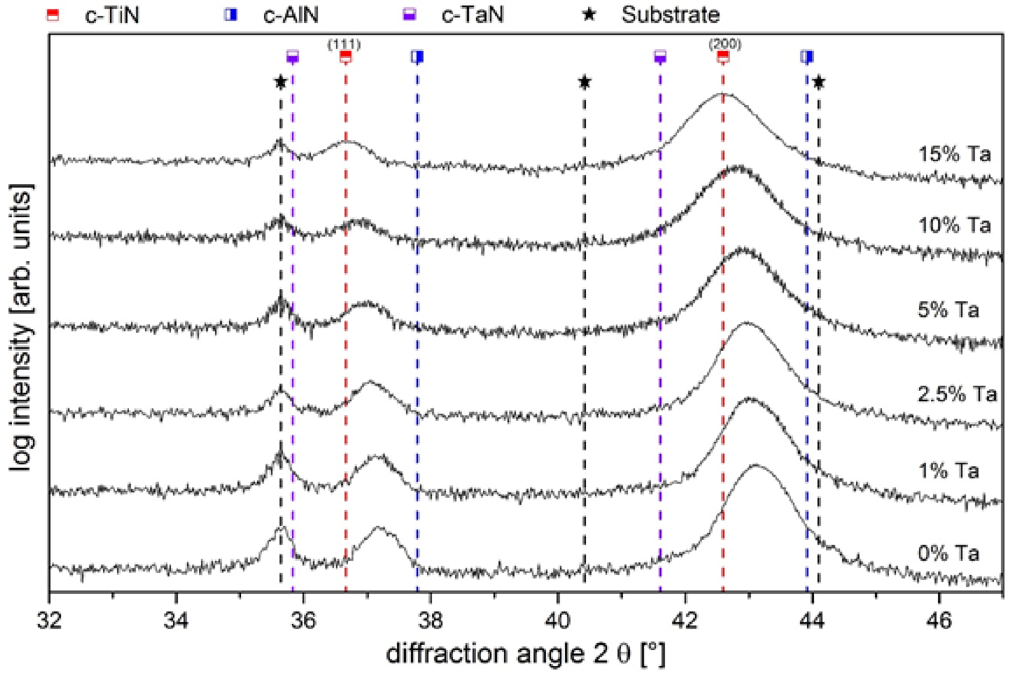

Figure 6.1: Grazing incidence X-ray diffractograms for as-deposited $(Ti_{1-x}Al_x)_{1-y}Ta_yN$ coatings deposited on cemented carbide substrates with SNUN geometry. The Ta content of the targets increases from bottom to top.

With increasing Ta content, the peaks shift towards lower diffraction angles, indicating a larger lattice spacing. This can be expected for the quaternary $(Ti_{1-x}Al_x)_{1-y}Ta_yN$ solid solution as the c-TaN lattice cell is bigger than that of c-TiN and c-AlN. Furthermore, the peak intensity decreases with increasing Ta content due to its higher absorption coefficient compared to the other elements of the system, resulting in a smaller intensity of the diffracted peaks [43].

6.1.2 Mechanical properties

The influence of an increasing Ta content on the hardness of as-deposited $(Ti_{1-x}Al_x)_{1-y}Ta_yN$ coatings is shown in Figure 6.2. The ternary $Ti_{1-x}Al_xN$ system exhibits a hardness of ~ 32.5 GPa. With increasing Ta content, a slight increase in hardness is detected, with a maximum value of ~ 34.5 GPa for the coating with 10 % Ta. This increase can be explained by the elastic distortion of the $Ti_{1-x}Al_xN$ lattice due to the incorporation of the larger Ta atoms. However, the effect is not very strong in the as-deposited state, as the misfit is small [9].

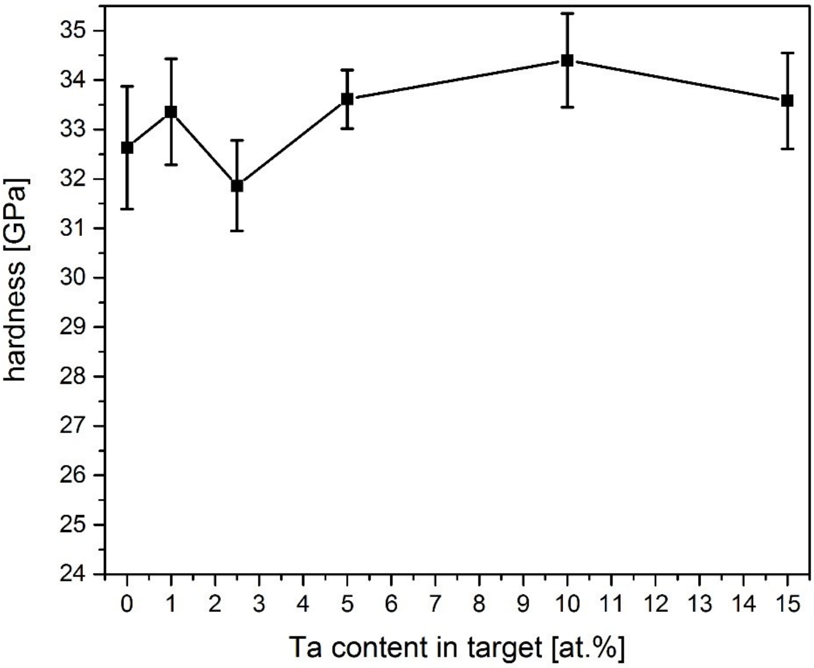

Figure 6.2: Hardness of as-deposited $(Ti_{1-x}Al_x)_{1-y}Ta_yN$ coatings with increasing Ta content.

6.1.3 Thermal stability

6.1.3.1 Powdered samples

DSC measurements were conducted on powdered samples to investigate thermally induced processes in the quaternary $(Ti_{1-x}Al_x)_{1-y}Ta_yN$ system without the influence of the substrate. Figure 6.3 shows the heat flow curves recorded during these measurements as a function of the temperature. Overall, three pronounced exothermic peaks can be observed: (*i*) the first one with a maximum between 700 and 750 °C, (*ii*) one with a maximum between 860 and 920 °C, which cannot be detected for the system with 15 % Ta, and (*iii*) one with its maximum between 1160 and 1220 °C. The position of the maximum of the third peak is shifted to higher temperatures with the Ta content increasing up to 5 % Ta, but decreases again for higher Ta contents. The intensity of all exothermic peaks decreases with increasing Ta content, indicating a lower loss of energy and therefore, a smaller fraction of the system undergoing the reaction. Furthermore, endothermic features can be observed for the systems with 10 % and 15 % Ta at temperatures above 1200 °C.

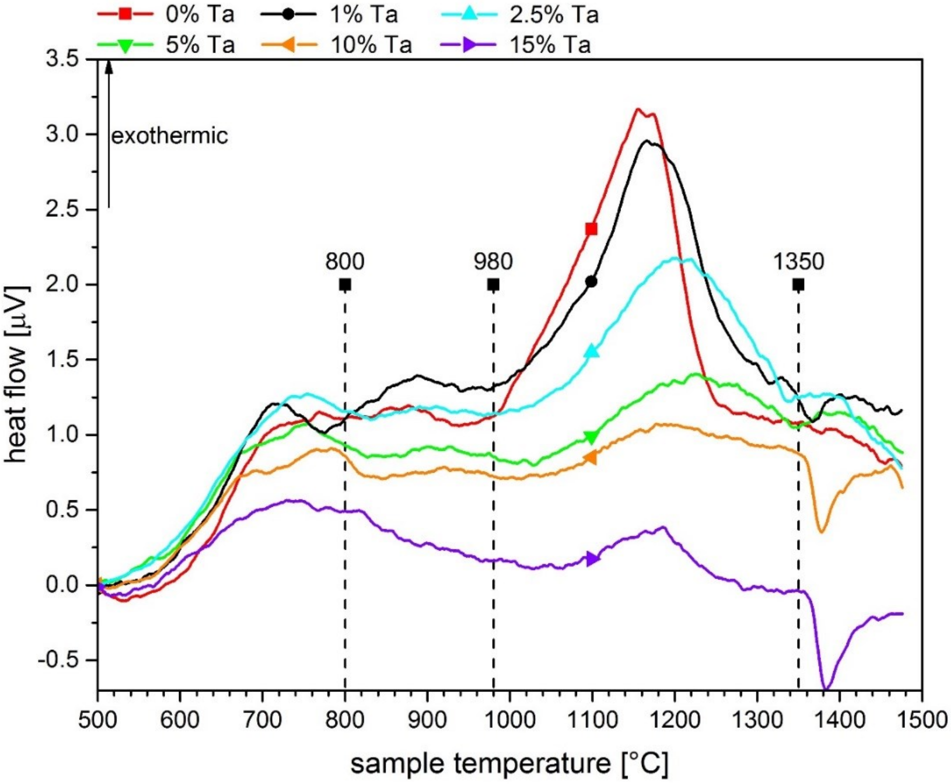

Figure 6.3: Heat flow recorded during qualitative DSC measurements of six powders with increasing Ta content. Three annealing temperatures, indicated in the diagram, were chosen to correlate the measured features with microstructural changes.

To further investigate the different partial reactions revealed by DSC, three temperatures were selected for additional annealing treatments of the powder samples. Subsequent to the annealing, the powders were investigated using XRD. The resulting diffractograms for each composition are presented in Figures 6.4a to f.

The powder of the ternary $Ti_{1-x}Al_xN$ system shows a single phase cubic microstructure at RT with slightly asymmetric peaks (Figure 6.4a), which can be explained by the change of the bias voltage during the deposition. Since the bias voltage affects the formation of residual stresses in the coating, its variation results in a gradually changing lattice spacing of the coating [11]. Hence, the recorded peak can be described as the sum of peaks from regions with slightly different lattice constants and thus peak positions. After annealing at 800 °C, a small peak shift towards higher diffraction angles can be observed, while the peak becomes narrower. These changes can be correlated with recovery processes, during which intrinsic stresses are reduced and the defect density decreases. Due to the nature of a powder, those residual stresses can only be of second or third order. The recovery processes are already in an advanced stage at this temperature, therefore, the first exothermic peak of the DSC signal can be attributed to recovery. Additionally, first signs of spinodal decomposition can be detected. The shoulders on the left side of the $Ti_{1-x}Al_xN$ peaks indicate the presence of c-TiN rich areas, which form spontaneously in the system from local fluctuations of the composition. The shoulders on the right side of the peaks due to c-AlN rich domains are less pronounced. After annealing at 980 °C, the positions of the $Ti_{1-x}Al_xN$ peaks are very close to the standard peak positions of c-TiN, which indicates that the decomposition process is almost completed. This correlates well with the second exothermic peak of the DSC measurements, which shows that the biggest part of the reaction enthalpy has been released at 980 °C. As the formed c-AlN is not stable and the annealing temperatures are high enough to enable diffusion, the stable w-AlN starts to form. The decomposition of the $Ti_{1-x}Al_xN$ solid solution and the formation of w-AlN are completed for the powder annealed at 1350 °C. When comparing the microstructure with the heat flow rate recorded during the DSC measurement, the formation of w-AlN is described by the third and largest exothermic peak. There is no substantive change of the microstructure detectable after annealing at 1500 °C.

Alloying the system with 1 % and 2.5 % Ta does not change the reaction of the material to annealing in a profound way, but retards certain processes as shown in Figures 6.4b and c. At RT, the peak positions shift to lower angles due to the incorporation of the large Ta atoms into the solid solution, as already discussed before (Figure 6.1). Decomposition is detectable for the two systems after annealing at 800 °C, but the shoulders are less pronounced compared to the ternary $Ti_{1-x}Al_xN$ system, indicating a less advanced decomposition process. Two explanations can be given for this behavior: First, the incorporation of the large Ta induces additional residual stress in the system and thus impedes diffusion, while secondly, the driving force of the decomposition is weakened by alloying with Ta [9, 28].

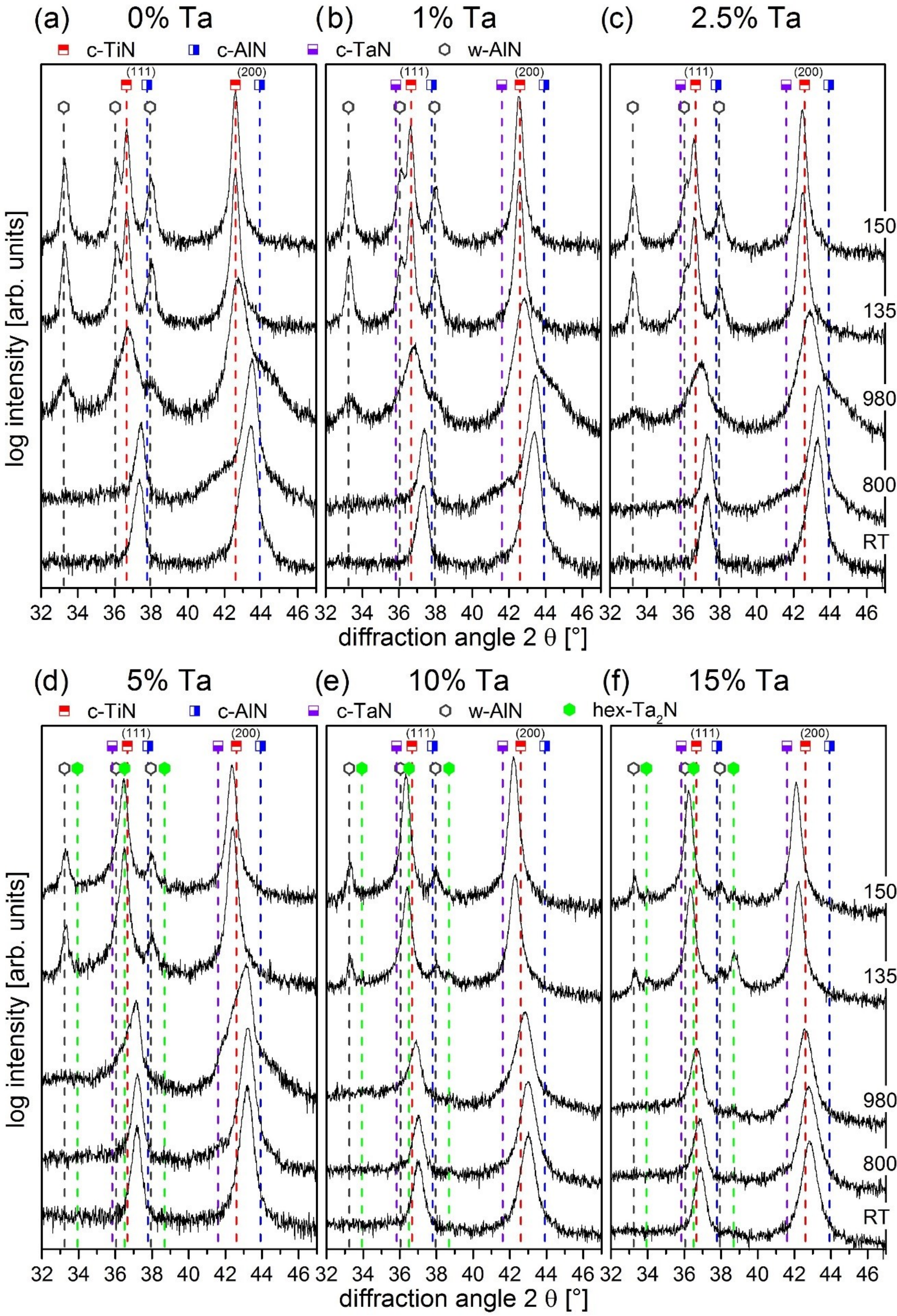

Figure 6.4: X-ray diffractograms for powdered samples with (a) 0% Ta, (b) 1 % Ta, (c) 2.5 % Ta, (d) 5 % Ta, (e) 10 % Ta, (f) 15 % Ta before annealing (RT), after annealing at selected temperatures (800, 980 and 1350 °C) and after the DSC measurement (1500 °C).

For the powders annealed at 980 °C, progressed decomposition can be observed, however, not as progressed as in the ternary $Ti_{1-x}Al_xN$ system, indicated by less pronounced shoulders of the $(Ti_{1-x}Al_x)_{1-y}Ta_yN$ peaks. Consequently, the shift of the matrix peaks towards lower diffraction angles is less pronounced. w-AlN is present after annealing at 980 °C for the two systems, but its content decreases with increasing Ta content. Due to the less advanced decomposition, less c-AlN is formed and thus, less transformation into the wurtzite structure is possible. The powders annealed at 1350 °C are fully decomposed, which is shown by the small width of the $(Ti_{1-x}Al_x)_{1-y}Ta_yN$ peaks and the peak positions, which are located between the standard peak positions of c-TiN and c-TaN. Furthermore, the fraction of w-AlN in the system is increased due to the higher annealing temperature. However, contrary to the ternary system, the formation of w-AlN is not finished, which is marked by the increasing intensity of the w-AlN peaks and the peak shift of the $(Ti_{1-x}Al_x)_{1-y}Ta_yN$ peaks towards lower angles after annealing at 1500 °C. This is in agreement with the heat flow curves recorded during the DSC measurements, where the temperature of the maximum of the third exothermic peak increases with increasing Ta content, indicating a retardation of the reaction to higher temperatures.

Figure 6.4d shows the diffractograms of the powder created from the coating with 5 % Ta. It exhibits a single phase cubic microstructure at RT and after annealing at 800 °C a small shoulder on the left side of the $(Ti_{1-x}Al_x)_{1-y}Ta_yN$ peaks appears. After annealing at 980 °C, shoulders on both sides of the matrix peaks can be observed, however, the peak positions shift only slightly towards lower angles. This is the effect of Ta on the system, which further retards the decomposition, compared to the powders with less Ta. Furthermore, a small w-AlN peak is detectable. Annealing at 1350 °C leads to full decomposition of the system and further formation of w-AlN. Compared to the powders shown in Figures 6.4a to c, less w-AlN is formed, also after annealing at 1500 °C. Hexagonal (hex-)Ta_2N precipitates can be detected for the coatings containing 5 % Ta after annealing at 1350 °C. This hex-Ta_2N is one of the stable nitrides formed by Ta [44] and has been reported by authors investigating $Al_{1-x}Ta_xN$ and $(Ti_{1-x}Al_x)_{1-y}Ta_yN$ systems [35, 45, 46]. However, no reports on the influence of this precipitate on mechanical properties can be found.

Increasing the Ta content in the system to 10 % and 15 % retards the decomposition process further as shown in Figures 6.4e and f, respectively. The w-AlN formation is also further retarded. A small peak is detectable for the system with 10 % Ta after annealing at 980 °C, while the coating with 15 % Ta first shows w-AlN after annealing at 1350 °C. For the latter, no indication for decomposition is detectable up to 1500 °C, which is confirmed by the missing second exothermic peak in the DSC measurement. At annealing temperatures higher than 980 °C, the $(Ti_{1-x}Al_x)_{1-y}Ta_yN$ peaks shift to lower angles due to the depletion of Al in the matrix resulting from the formation of w-AlN. While hex-Ta_2N only forms after annealing at 1350 °C for the coating with 5 % Ta, it is already present at 800 °C and RT for the coatings with 10 % and 15 % Ta, respectively. Koller *et al.* [45] showed that the formation of hex-Ta_2N is accompanied by a loss of nitrogen, which is represented by an endothermic reaction. This is in good agreement with the DSC measurements of the present work. The coatings containing 10 % and 15 % Ta show two endothermic peaks at temperatures above 1200 °C, where the first is superimposed by the exothermic formation of w-AlN. This superposition with the endothermic reactions also explains the apparent shift of the third exothermic peak to lower temperatures for the coatings with 10 % and 15 % Ta, which could not be explained by the microstructure. The peak intensity of hex-Ta_2N decreases again at temperatures above 1350 °C, which correlates with the second endothermic peak, indicating further release of nitrogen.

For a better overview of the peak shifts with respect to the different Ta contents and annealing temperatures, the out-of-plane lattice parameters of the c-phase were calculated from the diffraction angles using Bragg's law and the peak position of the (200) peak, which has the highest intensity. The lattice parameters of the powdered samples as well as the standard lattice parameters of c-TiN, c-AlN and c-TaN according to the respective ICDD files are summarized in Figure 6.5. It shows the increasing lattice parameter with increasing Ta content at RT, as already discussed in section 6.1.1. After annealing at 800 °C, recovery processes lead to a decrease of the lattice parameters. At 980 °C, spinodal decomposition affects the lattice parameter strongly, resulting in an increase. Decomposition is retarded with increasing Ta content and the increase of the lattice parameter becomes less pronounced, leading to the lowest lattice parameter for the sample with 5 % Ta. For the coatings with 10 % and 15 % Ta, the decomposition has a minor influence compared to the lattice distortion from the incorporation of the large Ta atoms. When annealing the ternary $Ti_{1-x}Al_xN$ system at higher temperatures than 800 °C, w-AlN forms and consequently the lattice parameter of the matrix increases, reaching the level of c-TiN. With increasing Ta content, the formation of w-AlN and thus, the increase of the lattice parameter is shifted to higher temperatures. For annealing temperatures higher than 1350 °C, the lattice parameter exceeds the level of c-TiN.

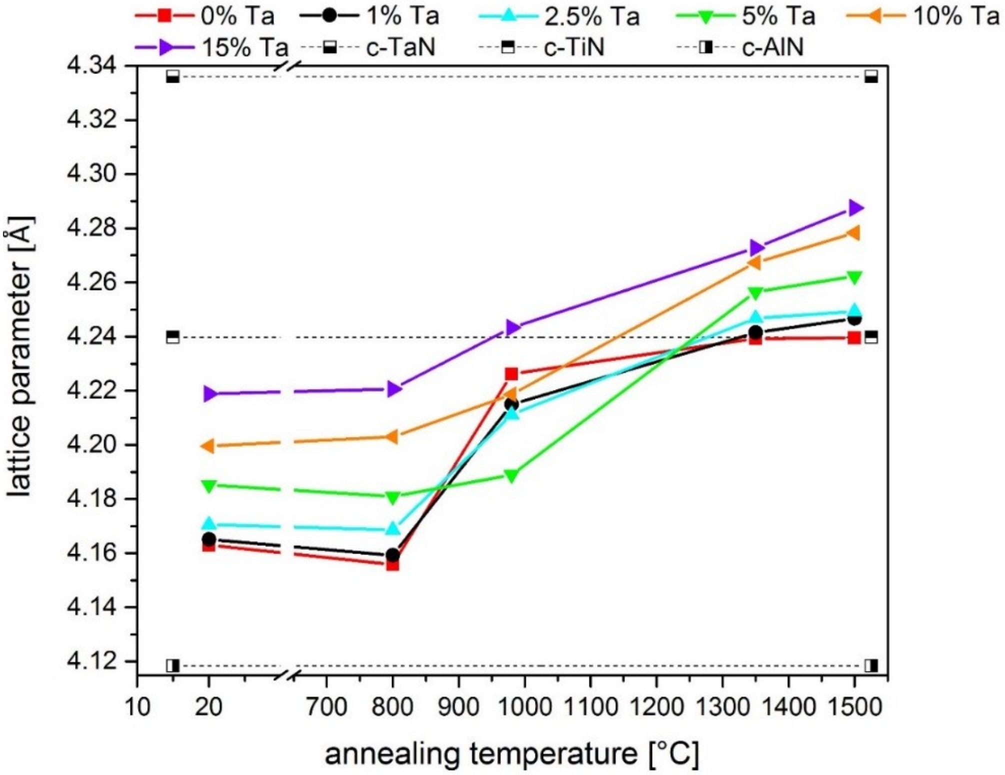

Figure 6.5: Evolution of the lattice parameter of powdered samples with increasing Ta content as a function of the annealing temperature. The standard lattice parameters of c-TaN, c-TiN and c-AlN are shown as well.

6.1.3.2 Microstructure of coatings on substrates

The evolution of the microstructure with increasing annealing temperature was additionally investigated on coatings deposited on cemented carbide substrates in SNUN geometry. Unlike the powdered coatings, these coatings are grown on the substrate material used for cutting tools and the influence of the substrate during annealing on the microstructural changes can be investigated. Thus, in contrast to the powdered samples, also stresses of first order play a role and the behavior of the coatings during the following annealing tests is closer to coatings during application. As temperatures up to 1000 °C can form locally during cutting applications [2], the coatings were annealed at temperatures between 700 and 1000 °C in steps of 50 °C. The small increment was chosen to investigate the evolution of microstructure and hardness, which were evaluated on the same coatings, in detail.

Figure 6.6a shows the diffractograms of the $Ti_{0.5}Al_{0.5}N$ coating, from bottom to top with increasing annealing temperature. Although the XRD measurements were performed with detector scan mode to minimize the substrate influence, one prominent peak of the cemented carbide substrate is detectable at approximately 35.7°. After annealing at 700 °C, the c-$Ti_{1-x}Al_xN$ peaks shift towards higher angles. This might not only be attributed to recovery processes but also to beginning decomposition and accompanied development of microstrain, as it has been shown that the initially formed domains are not detectable by XRD measurements due to their small size [23]. In contrast to the powdered samples, residual stresses of all three orders are relaxed during the recovery processes. Hence, the $Ti_{1-x}Al_xN$ peaks shift towards higher angles due to the recovery. Decomposition is indicated by shoulders forming on the c-AlN side of the $Ti_{1-x}Al_xN$ peaks and a slight peak shift towards higher diffraction angles after annealing at 750 °C. After annealing at 800 °C, c-TiN rich domains are detectable, leading to another decrease of the lattice parameter, indicated by the peak shift to higher angles. At annealing temperatures higher than 800 °C, the decomposition of the solid solution is more distinct and the peaks shift towards the standard peak position of the c-TiN lattice, with a pronounced shoulder indicating c-AlN rich domains. Transformation to w-AlN can be observed after annealing at 900 °C and its fraction increases with higher annealing temperatures.

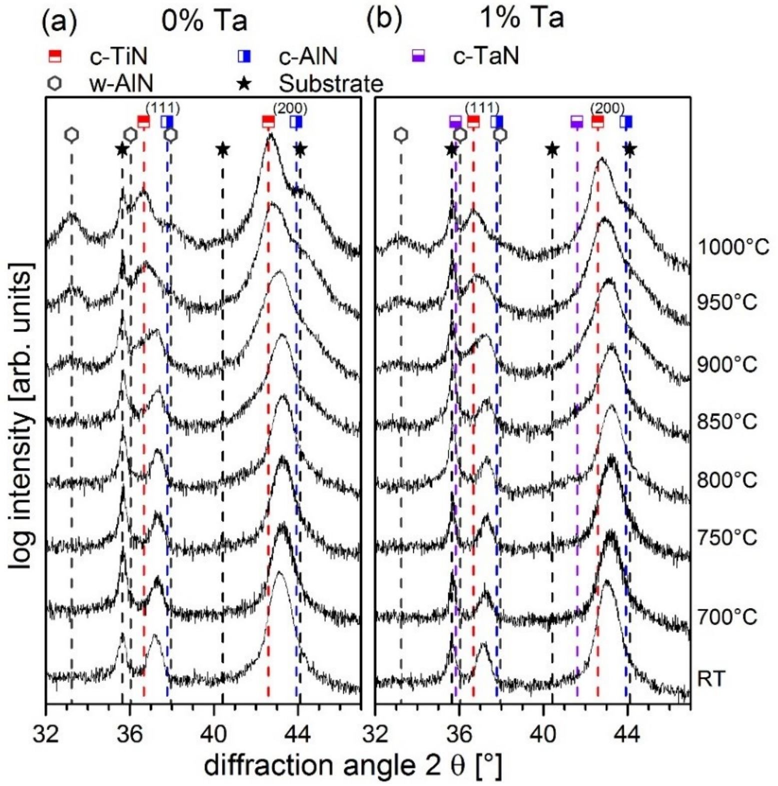

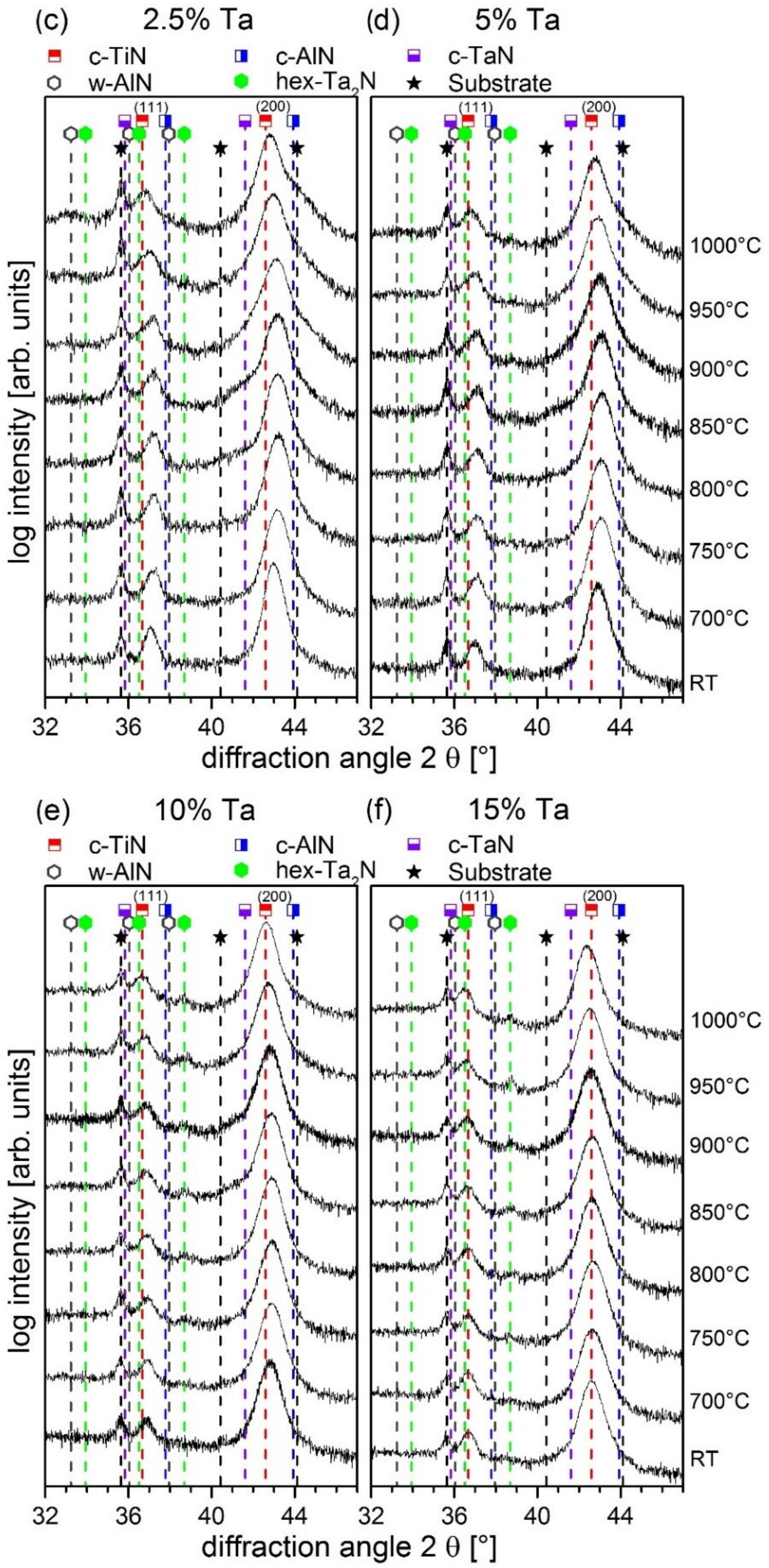

Figure 6.6: Grazing incidence X-ray diffractograms for coatings deposited on cemented carbide substrates with (a) 0 % Ta, (b) 1 % Ta, (c) 2.5 % Ta, (d) 5 % Ta, (e) 10 % Ta and (f) 15 % Ta before annealing (RT) and after annealing in a vacuum furnace.

The thermal stability of the coating containing 1 % Ta is indicated by the series of X-ray diffractograms in Figure 6.6b. The incorporation of Ta does not result in a shift of the decomposition and the formation of w-AlN to higher temperatures. Both processes can be detected at the same temperatures as for the coating without Ta. However, Ta still slows down both reactions, which is shown by the less pronounced c-AlN shoulder and the lower intensity of the w-AlN peak in Figure 6.6b compared to Figure 6.6a at annealing temperatures higher than 900 °C. Compared to the powdered samples, decomposition is less pronounced at 800 °C for the coatings.

The diffractograms of the coatings with 2.5 % and 5 % Ta are presented in Figures 6.6c and d and show a shift of the decomposition onset temperature to 800 and 850 °C, respectively. While a shoulder is first detectable on the c-AlN side for the coatings with 0 % and 1 % Ta, the formation of c-TiN domains is more pronounced for the coatings with 2.5 % and 5 % Ta. Additionally, the formation of w-AlN shifts to 950 °C and its amount decreases with increasing Ta content. hex-Ta_2N peaks are visible after annealing at 900 and 850 °C for the coatings with 2.5 % and 5 % Ta respectively, which differs from the powdered samples, where no hex-Ta_2N could be found for the coating with 2.5 % Ta and first precipitates were observed at 1350 °C for the coating with 5 % Ta.

Figures 6.6e and f show the microstructural evolution of the coatings with 10 % and 15 % Ta, respectively, with temperature. For the coating with 10 % Ta, the onset temperatures of decomposition and w-AlN formation stay the same as for the coating with 5 % Ta, but the formation of hex-Ta_2N starts already at 700 °C. Furthermore, the decomposition is less pronounced, compared to the coatings with less Ta. This is marked by the smaller overall shift of the $(Ti_{1-x}Al_x)_{1-y}Ta_yN$ peaks and the decreased peak width at annealing temperatures higher than 850 °C. The coating with 15 % Ta shows very weak decomposition after annealing at 900 °C and the w-AlN formation is shifted to 1000 °C. Only a slight shift of the $(Ti_{1-x}Al_x)_{1-y}Ta_yN$ peaks to lower angles is observed up to 900 °C and their positions for higher annealing temperatures are located between the standard peak positions of c-TiN and c-TaN. The powdered coatings with 15 % Ta showed no decomposition up to annealing temperatures of 1500 °C. Comparing the peak positions for the same annealing temperatures in Figures 6.4f and 6.6f evidences that all peaks of the coatings are shifted to smaller angles, indicating larger out-of-plane lattice constants. These can be explained by higher compressive residual stress parallel to the substrate, which retards diffusion and, consequently, decomposition processes [28]. Similarly to the powdered samples, hex-Ta_2N is already detectable in the as-deposited coating.

6.1.3.3 Mechanical properties

Figure 6.7 shows the hardness of the coatings deposited on cemented carbide substrates using the BG parameter set with Ta contents from 0 % to 15 % as a function of the annealing temperature. The ternary $Ti_{0.5}Al_{0.5}N$ system has a hardness of ~ 32.5 GPa in the as-deposited state, which increases to ~ 34 GPa after annealing at 700 °C. For higher annealing temperatures, the hardness decreases, reaching a minimum of ~ 25 GPa after annealing at 1000 °C. When comparing the hardness with the microstructure determined by the X-ray diffractograms shown in Figure 6.6a, the hardness maximum correlates with the onset of decomposition. Furthermore, w-AlN is formed after annealing at 900 °C, which is in good agreement with the hardness drop.

The $Ti_{0.495}Al_{0.495}Ta_{0.01}N$ coating has a hardness of ~ 33 GPa in the as-deposited state, which stays constant up to an annealing temperature of 850 °C. Annealing at higher temperatures results in a decreasing hardness. The minimum value of ~ 29 GPa is measured after annealing at 1000 °C. According to the X-ray diffractograms shown in Figure 6.6b, decomposition starts at 750 °C for this sample, explaining the high hardness values for this annealing temperature. The hardness drop after annealing at 900 °C can be attributed to the formation of w-AlN. Up to annealing temperatures of 900 °C, the hardness values are very similar to the ternary system, whereas even higher temperatures lead to a higher hardness of the $Ti_{0.495}Al_{0.495}Ta_{0.01}N$ sample.

The coating containing 2.5 % Ta has a hardness of ~ 32 GPa in the as-deposited state and after annealing at 700 °C. For higher annealing temperatures, the hardness reaches a maximum value of ~ 33 GPa after annealing at 800 °C and decreases again for even higher annealing temperatures. The minimum hardness of ~ 30 GPa is measured again after annealing at 1000 °C. The onset of decomposition is detectable by XRD at 800 °C (see Figure 6.6c) and correlates well with the maximum hardness. The increased Ta content results in higher hardness values for annealing temperatures higher than 900 °C compared to the previously discussed coatings.

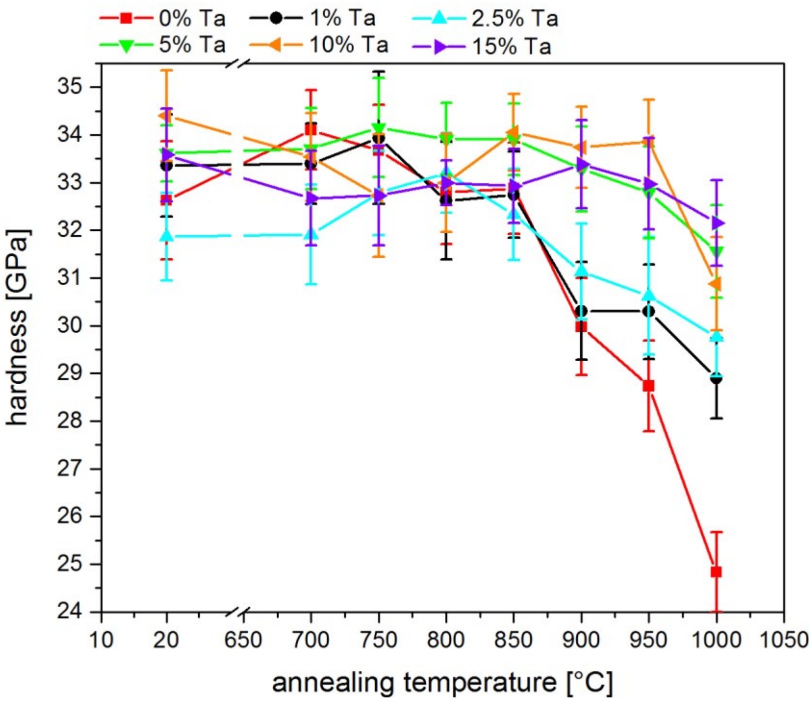

Figure 6.7: Hardness evolution as a function of annealing temperatures of $(Ti_{1-x}Al_x)_{1-y}Ta_yN$ coatings with increasing Ta contents grown on cemented carbide substrates.

Alloying the coating with 5 % Ta leads to an increase of the hardness to ~ 33.5 GPa in the as-deposited state. This value is maintained for annealing temperatures up to 900 °C and decreases to 31.5 GPa for higher temperatures. Comparing the hardness with the microstructure determined utilizing XRD shows that Ta retards decomposition to 850 °C and w-AlN formation to 950 °C. Since the microstructure of the coating does not change up to these temperatures, the high hardness values are also maintained.

$Ti_{0.45}Al_{0.45}Ta_{0.1}N$ coatings exhibit a hardness of ~ 34.5 GPa in the as-deposited state. When annealed at temperatures between 700 and 950 °C, the hardness decreases and remains at ~ 33.5 GPa. It further decreases to ~ 31 GPa after annealing at 1000 °C. Similar to the sample with 5 % Ta, the decomposition is retarded to 850 °C, according to the diffractograms shown in Figure 6.6e. Due to the formation of w-AlN after annealing at 950 °C, the hardness decreases considerably at even higher annealing temperatures.

The sample with 15 % Ta shows a hardness of ~ 33.5 GPa in the as-deposited state, which decreases to ~ 33 GPa for annealing temperatures up to 1000 °C. Alloying the coating with this amount of Ta results in a high onset temperature for decomposition and a much less pronounced decomposition, as depicted in Figure 6.6f. Consequently, microstructure and hardness do not change significantly during annealing up to 1000 °C. The three coatings with the highest Ta content (i.e. 5 %, 10 % and 15 % Ta) have the highest hardness values for annealing temperatures above 900 °C. Furthermore, the values are very similar in the temperature range between 900 and 1000 °C. This evidences that Ta addition improves the mechanical properties of $Ti_{0.5}Al_{0.5}N$ at high temperatures by retarding decomposition of the matrix and formation of w-AlN. Another feature these three coatings have in common is the precipitation of hex-Ta_2N. Due to its high hardness [47], it can be assumed that this precipitate can positively affect the mechanical properties of the alloyed system at high temperatures. Precipitation hardening is one of the most effective mechanisms to enhance mechanical properties at high temperatures, as the particles can pin dislocations and therefore impede diffusion [19].

The hardness measurements presented in this thesis are in good agreement with literature [28, 45]. Koller *et al.* [45] observed hardness values of ~ 32 GPa in the as-deposited state for $Ti_{0.54}Al_{0.46}N$ and $Ti_{0.45}Al_{0.36}Ta_{0.19}N$ coatings synthesized using CAE with V_B = -40 V , showing no evidence for solid solution hardening. After annealing at 1000 °C, the hardness of the ternary system decreased to 22 GPa, while the hardness of the quaternary system increased to 37 GPa. The higher hardness values for the coatings in the present thesis can be explained by the higher Al content (see section 4.1) and bias voltage. Latter typically results in a higher compressive residual stress and smaller grain size, which consequently increases the hardness due to grain boundary strengthening [19, 48, 49]. The maximum hardness of 37 GPa at 1000 °C is by 4 GPa higher than the hardness of the $Ti_{0.425}Al_{0.425}Ta_{0.15}N$ coating in the present theses at the same temperature; this can be explained by the even higher Ta content studied in the literature, which further increases the hardness at high temperatures. Rachbauer *et al.* [28] reported on $(Ti_{0.4}Al_{0.6})_{1-y}Ta_yN$ coatings with $y \leq 0.1$ deposited by unbalanced magnetron sputtering. They showed that alloying the system with y = 0.1 retards the decomposition by ~ 200 – 300 °C to ~ 1200 °C. Furthermore, it resulted in a hardness increase from ~ 30 to ~ 40 GPa for the as-deposited coatings and from ~ 38 to ~ 42 GPa after annealing at 900 °C. The coatings presented in this thesis have a lower Al content, which explains the overall lower hardness values. Additionally, the age hardening of the ternary system is more pronounced for higher Al contents [50].Arc evaporated coatings have also been reported to be less hard than coatings deposited by sputtering as macro particles deteriorate the mechanical properties [12].

6.2 Bias voltages

The influence of three deposition parameter sets with varying bias voltages on the thermal stability of the $(Ti_{1-x}Al_x)_{1-y}Ta_yN$ system was investigated on coatings deposited on cemented carbide substrates with SNUN geometry. For this purpose, the coatings were annealed at temperatures from 700 °C up to 1000 °C in steps of 50 °C and subsequently investigated utilizing XRD. Two coating compositions were used, namely $Ti_{0.5}Al_{0.5}N$ and $Ti_{0.475}Al_{0.475}Ta_{0.05}N$. Additionally, nanoindentation measurements were conducted to correlate the microstructural evolution to changes of mechanical properties.

6.2.1 Microstructure

Figure 6.8a shows the diffractograms of the $Ti_{0.5}Al_{0.5}N$ coatings deposited using a constant bias voltage of -40 V. The peak shift and narrowing after annealing at 700 °C can be explained by recovery, while decomposition is first detected at 750 °C. There, a low but very broad shoulder is detectable at the left hand side of the (200) $Ti_{1-x}Al_xN$ peak. After annealing at higher temperatures, the shoulder becomes more pronounced. Due to the decomposition, the $Ti_{1-x}Al_xN$ peaks shift towards higher diffraction angles with increasing annealing temperature. At 800 °C, c-AlN rich domains start to form. The associated peaks are detected at angles higher than the standard peak position of c-AlN, indicating a smaller lattice spacing. At annealing temperatures higher than 800 °C, the effect of decomposition on the peak position becomes more significant and the $Ti_{1-x}Al_xN$ peaks shift towards lower diffraction angles. However, decomposition is not yet finished at 1000 °C. Formation of w-AlN starts after annealing at 900 °C.

The coating with the same target composition but deposited applying a bias voltage of -100 V is shown in Figure 6.8b. Overall, the peaks are lower and broader compared to the coating in Figure 6.8a, which indicates a smaller domain size and a larger microstrain. Both effects are results of the higher energies of bombarding ions during the deposition process due to the higher bias voltage [51]. In addition, the peaks of the as-deposited coatings are shifted to lower angles compared to the coating grown with V_B = -40 V, implying a larger out-of-plane lattice parameter. This is in good agreement with literature, since a higher bias voltage typically results in higher compressive residual stress [49, 52].

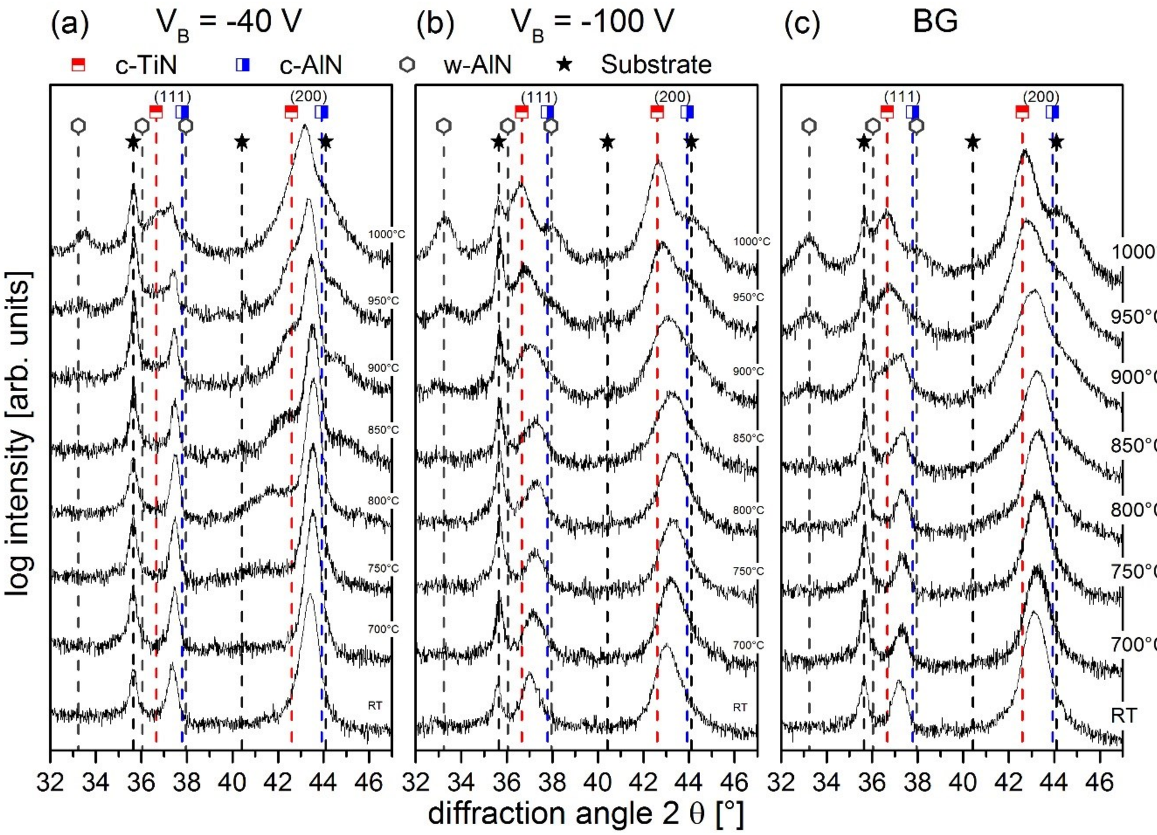

Figure 6.8: Grazing incidence X-ray diffractograms for $Ti_{0.5}Al_{0.5}N$ *coatings deposited with the bias voltage* (V_B) *sets (a)* V_B = -40 V, *(b)* V_B = -100 V *and (c) BG (= bias gradient) on cemented carbide substrates before annealing (RT) and after annealing in a vacuum furnace.*

The peak shift to higher diffraction angles after annealing at 700 °C is higher compared to the coatings deposited at a bias voltage of -40 V, indicating more pronounced recovery processes. A higher defect density and thus, a higher microstrain in the as-deposited coatings represents the driving force for this behavior. Compared to the coating deposited at the lower bias voltage, the decomposition onset temperature is increased to 800 °C, which is in good agreement with literature [48]. The formation of w-AlN starts at 850 °C, which is lower than for the coating grown at V_B = -40 V. This is a consequence of the higher amount of nucleation sites due to a finer grained microstructure [53]. The decomposition is finished after annealing at 1000 °C.

Figure 6.8c shows the diffractograms of $Ti_{0.5}Al_{0.5}N$ coatings deposited applying a bias voltage of -40 V for the zone close to the interface to the substrate and increasing it to -70 V close to the surface. Decomposition starts at 750 °C, indicated by the shoulders forming on the c-AlN side of the $Ti_{1-x}Al_xN$ peaks, and is finished after annealing at 1000 °C. Formation of w-AlN starts after annealing at 900 °C and the amount is comparable to the coating deposited at the high bias voltage. The bias voltage lies between those of the coatings described earlier and the shape and position of the measured peaks as well as the thermal evolution of these characteristics are a mixture of the previously described. While the peak intensity of the (200) peak is comparable to the coating deposited at the low bias voltage, it is very broad. The bias gradient gradually changes the lattice parameters of the coating, as discussed in section 6.1.3, which can explain the broadening of the peak. This also correlates well with the large peak shift observed after annealing at 700 °C, suggesting that this system has the strongest recovery of the three coatings described.

The influence of different deposition parameter sets on the thermal stability of the $Ti_{0.475}Al_{0.475}Ta_{0.05}N$ system is shown in Figures 6.9a to c. No substrate peak is detectable for the as-deposited coatings grown at V_B = -40 V and V_B = -100 V, however, both coatings were synthesized on cemented carbide substrates. The microstructural reaction to annealing of the coating deposited at V_B = -40 V is visualized in Figure 6.9a. Recovery processes influence the sample only slightly and the resulting peak shift towards higher angles after annealing at 700 °C is small. The decomposition onset temperature is 800 °C, where shoulders on the left hand side of the $(Ti_{1-x}Al_x)_{1-y}Ta_yN$ peaks are observed. With increasing annealing temperature, these shoulders become more pronounced. c-AlN domains are first detected after annealing at 850 °C. Despite ongoing decomposition, indicated by the shoulders developing on both sides of the $(Ti_{1-x}Al_x)_{1-y}Ta_yN$ peaks, the peak positions of the matrix remain at an almost constant diffraction angle up to annealing temperatures of 1000 °C. The formation of w-AlN starts at 1000 °C and hex-Ta_2N can be detected in all annealed coatings, with its peak intensity increasing with rising annealing temperatures. Compared to the ternary $Ti_{0.5}Al_{0.5}N$ system represented in Figure 6.8a, all thermally induced processes are retarded. This effect can be attributed to the alloying with Ta, as discussed in section 4.3.

Figure 6.9b presents diffractograms of $Ti_{0.475}Al_{0.475}Ta_{0.05}N$ coatings, deposited while applying a bias voltage of -100 V. A peak shift towards higher angles can be observed for the coating annealed at 700 °C, which can be attributed to recovery. Decomposition is first discernible after annealing at 900 °C, indicated by shoulders forming at the c-AlN side of the $(Ti_{1-x}Al_x)_{1-y}Ta_yN$ peaks. The formation of w-AlN starts at 1000 °C, where a small peak is detected. hex-Ta_2N can be found in the as-deposited coating as well as in all annealed coatings. When comparing the diffractograms to those of the coating which was synthesized with a lower bias voltage, the same relation can be found as in the ternary systems. The (200) peak is smaller, broader and shifted to lower angles, indicating a smaller domain size and higher micro- and macrostrain in the coating deposited at V_B = -100 V. Consequently, recovery processes are more pronounced and the peak shift towards higher angles after annealing at 700 °C is more distinct. The decomposition onset temperature of 900 °C is higher than for the coating deposited at a low bias voltage. c-AlN domains are detectable first, which indicates higher compressive residual stresses in this coating [53]. When comparing the diffractograms in Figure 6.8b and 6.9b, the effect of alloying Ta to the system is evident. It is responsible for the overall peak shift towards lower angles at RT and retards the decomposition and w-AlN formation. Therefore, both processes are not completed after annealing at 1000 °C for the $Ti_{0.475}Al_{0.475}Ta_{0.05}N$ system.

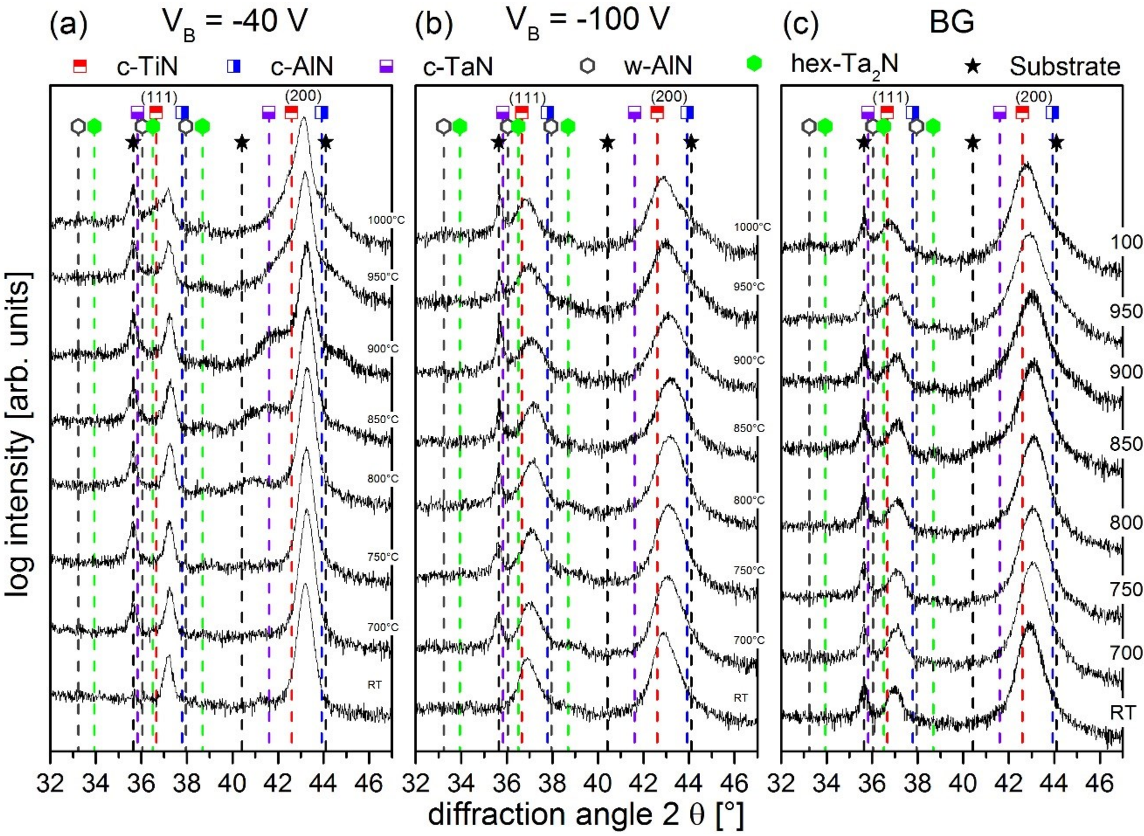

Figure 6.9: Grazing incidence X-ray diffractograms for $Ti_{0.475}Al_{0.475}Ta_{0.05}N$ coatings deposited with the bias voltage (V_B) sets (a) V_B = -40 V, (b) V_B = -100 V and (c) BG (= bias gradient) on cemented carbide substrates before annealing (RT) and after annealing in a vacuum furnace.

Diffractograms of the $Ti_{0.475}Al_{0.475}Ta_{0.15}N$ system synthesized with the BG parameter set are shown in Figure 6.9c. Recovery processes and decomposition are detectable after annealing at 700 and 800 °C, respectively. Formation of w-AlN is first observed after annealing at 950 °C and hex-Ta_2N forms at temperatures higher than 850 °C. Similarly to the ternary system shown in Figure 6.8, the thermal stability of the $Ti_{0.475}Al_{0.475}Ta_{0.05}N$ coating deposited with the

BG parameter set is comparable to that of the coatings deposited at constant bias voltages. While the peak intensity of the (200) peak is almost as high as for the coating deposited at the low bias voltage, the peak is broader due to the changed bias voltage and, consequently, lattice parameter. Furthermore, it is located at lower angles than the $(Ti_{1-x}Al_x)_{1-y}Ta_yN$ peaks of the coatings shown in Figures 6.9a and b, indicating higher compressive residual stress. Recovery processes are as strong as in the coating deposited at a bias voltage of -100 V, however, the decomposition onset temperature of 800 °C lies between the values of the other two coatings. The formation of w-AlN starts at lower temperatures than for the coatings grown at V_B = -40 V and V_B = -100 V, while the precipitation of hex-Ta_2N is retarded to higher temperatures.

6.2.2 Mechanical properties

Figure 6.10a shows the hardness evolution of $Ti_{0.5}Al_{0.5}N$ coatings grown with different bias voltages on cemented carbide substrates as a function of the annealing temperature. The hardness of the coating deposited at V_B = -40 V is ~ 28 GPa in the as-deposited state and ~ 33 GPa for the coatings synthesized at V_B = -100 V and applying a bias gradient. The high hardness of the latter coatings can be explained by more densely packed grain boundaries, as inferred by the SZD described by Anders [16]. Furthermore, a higher compressive residual stress and smaller grain size can be expected for coatings grown at higher bias voltages [48, 49]. Additionally, the lattice parameter of the system changes during the deposition process due to the bias gradient, which induces strain to the system. All of these effects result in a hardness increase.

The hardness of the coating deposited at V_B = -40 V stays constant up to annealing temperatures of 700 °C. After annealing at 750 °C, it increases to ~ 30 GPa. This hardness increase correlates with the starting decomposition of the system detected by XRD (Figure 6.8a), and thus the formation of coherency strain [33]. For higher annealing temperatures, the hardness decreases and reaches a minimum level of ~ 24 GPa after annealing at 950 °C. The hardness decrease can be explained by the proceeding decomposition of the supersaturated solid solution towards its stable constituents c-TiN and w-AlN. Latter is detected in the system after annealing at 900 °C.

The $Ti_{0.5}Al_{0.5}N$ coating deposited at V_B = -100 V has a hardness of ~ 31.5 GPa for annealing temperatures between 700 and 900 °C. For higher temperatures, the hardness decreases to ~ 27 GPa, reaching its lowest value after annealing at 1000 °C. Decomposition starts after annealing at 800 °C, as shown in the X-ray diffractograms in Figure 6.8b, which explains why the hardness does not decrease strongly up to this temperature. Formation of w-AlN after annealing at 850 °C contributes to the measured hardness decline at annealing temperatures above 900 °C.

The $Ti_{0.5}Al_{0.5}N$ coatings deposited applying an increasing bias voltage have a hardness maximum of ~ 34 GPa after annealing at 700 °C. The hardness stays between the hardness of the as-deposited coatings of ~ 33 GPa and the maximum hardness up to annealing temperatures of 850 °C. For higher annealing temperatures, it considerably decreases, reaching the lowest value of ~ 25 GPa after annealing at 1000 °C. Comparing the three coatings synthesized with different bias voltage sets, the BG parameter set results in the highest hardness values for annealing temperatures up to 850 °C. The above mentioned changing lattice parameters can contribute to the high hardness of the system at low temperatures. The formation of w-AlN starts at 850 °C, which correlates with the hardness decrease.

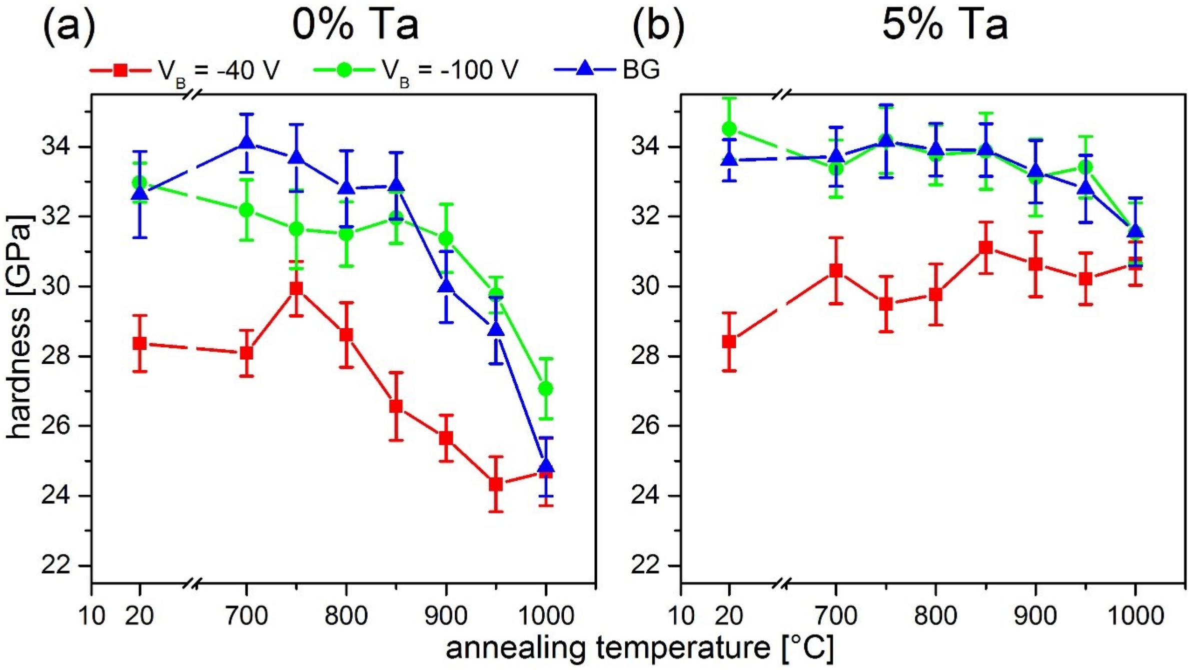

Figure 6.10: Hardness evolution as a function of vacuum annealing treatments of (a) $Ti_{0.5}Al_{0.5}N$ *and (b)* $Ti_{0.475}Al_{0.475}Ta_{0.05}N$ *coatings grown on cemented carbide substrates. The influence of a changed bias voltage* (V_B) *is shown for both systems (BG = bias gradient).*

Figure 6.10b shows the hardness of the $Ti_{0.475}Al_{0.475}Ta_{0.05}N$ coating deposited using the three different bias voltage sets as a function of the annealing temperature. The coating grown at V_B = -40 V has a hardness of ~ 28 GPa in the as-deposited state, while the coatings deposited at V_B = -100 V and with the BG parameter set both have a hardness of ~ 34 GPa. As discussed above, the higher bias voltage and the bias gradient result in higher hardness levels. Compared to the ternary system, the hardness does not change for the coating synthesized at V_B = -40 V and is ~ 1 GPa higher for the other two deposition parameter sets. The increase of the hardness can be explained by the incorporation of Ta into the matrix (see section 6.1.2).

$Ti_{0.475}Al_{0.475}Ta_{0.05}N$ coatings exhibit a constant hardness level of ~ 30 GPa after annealing at temperatures between 700 and 1000 °C. Compared to the $Ti_{0.5}Al_{0.5}N$ coating, the hardness values are similar up to annealing temperatures of 800 °C. For higher annealing temperatures, the hardness is higher for the coating alloyed with 5 % Ta. According to the XRD measurements shown in Figure 6.9a, decomposition of the system is shifted to 800 °C and w-AlN formation starts after annealing at 1000 °C, which explains the high hardness values up to this temperature.

The coating synthesized at V_B = -100 V has a hardness of ~ 34 GPa for annealing temperatures up to 900 °C. With higher annealing temperatures, the hardness slightly decreases, exhibiting the lowest value (~ 31.5 GPa) after annealing at 1000 °C. In Figure 6.9b, decomposition of the metastable solid solution and formation of w-AlN can be detected at 900 and 1000 °C for the $Ti_{0.475}Al_{0.475}Ta_{0.05}N$ coating grown at V_B = -100 V. These temperatures are higher compared to those obtained for the $Ti_{0.5}Al_{0.5}N$ coating deposited at the same bias voltage. Alloying with Ta retards decomposition and formation of w-AlN, resulting in a higher hardness at annealing temperatures exceeding 900 °C.

The hardness of the $Ti_{0.475}Al_{0.475}Ta_{0.05}N$ coating deposited with increasing bias voltage remains constant up to annealing temperatures of 950 °C. For higher annealing temperatures, it decreases to ~ 31.5 GPa. The diffractograms of this system are presented in Figures 6.9c and show broad peaks, resulting from changing lattice parameters due to the bias gradient, and starting decomposition after annealing at 800 °C. The combination of these two effects explains the high hardness in the as-deposited state and at high temperatures. Furthermore, the transformation to w-AlN starts after annealing at 950 °C but is not very pronounced. Consequently, the hardness decrease is small.

7 Summary and conclusions

In the present thesis, the effect of Ta alloying on the microstructure, mechanical properties and thermal stability of $Ti_{1-x}Al_xN$ hard coatings with a constant Ti/Al atomic ratio of 50/50 is investigated for coatings synthesized using cathodic arc evaporation. Powder metallurgically prepared targets with Ta content increasing from 0 % to 15 % were used for the deposition of coatings on cemented carbide substrates and mild steel foil. During the deposition process, the bias voltage was gradually increased from -40 V at the interface to the substrate to -70 V at the coating surface. A single phase cubic microstructure is observed for the as-deposited coatings, independent from the Ta content. The addition of Ta results in a hardness increasing from ~ 32.5 GPa for the ternary $Ti_{0.5}Al_{0.5}N$ system to ~ 34.5 GPa for the system alloyed with 10 % Ta. Differential scanning calorimetry measurements and subsequent X-ray diffraction of powdered coatings reveal that the decomposition of the $Ti_{1-x}Al_xN$ solid solution and formation of w-AlN are retarded by the increasing Ta content. For $Ti_{0.425}Al_{0.425}Ta_{0.15}N$, no decomposition is observed up to 1500 °C. Additionally, hex-Ta_2N, a hard and stable precipitate, is formed in the samples containing 5 %, 10 % and 15 % Ta. The microstructure and mechanical properties of coatings on cemented carbide substrates after vacuum annealing at temperatures between 700 and 1000 °C were investigated using XRD and nanoindentation, respectively. The onset temperature for decomposition is shifted from 750 °C for the ternary system to 900 °C for the coating containing 15 % Ta. Furthermore, w-AlN formation is retarded from 900 °C to 1000 °C. Consequently, the hardness of the coatings containing Ta is higher after annealing. At 1000 °C, the hardness of $Ti_{0.425}Al_{0.425}Ta_{0.15}N$ is ~33 GPa, which is ~ 8 GPa higher than the value for $Ti_{0.5}Al_{0.5}N$.

Furthermore, the deposition process was altered for selected coatings by changing the applied bias voltage to investigate its influence on the thermal stability of samples within the $(Ti_{1-x}Al_x)_{1-y}Ta_yN$ system. X-ray diffraction measurements of vacuum annealed $Ti_{0.5}Al_{0.5}N$ and $Ti_{0.475}Al_{0.475}Ta_{0.05}N$ coatings show that increasing the bias voltage from -40 V to -100 V results in a retardation of decomposition. Additionally, the formation of w-AlN is shifted to lower temperatures for the ternary coating. This can be explained by a higher number of nucleation sites due to a smaller grain size. Applying a bias gradient during deposition results in gradually changed lattice parameters in the synthesized coating and consequently in the formation of coherency strains. Nanoindentation of vacuum annealed coatings shows that the hardness of the coating synthesized at V_B = -100 V is higher for annealing temperatures up to 1000 °C, which can be explained by a smaller grain size and retarded formation of w-AlN. The mechanical properties of the coatings deposited while increasing the bias voltage are similar to those of the coatings deposited at V_B = -100 V. Alloying with 5 % Ta results in a higher hardness at annealing temperatures exceeding 800 °C, where the formation of w-AlN is retarded and hex-Ta_2N precipitation promoted.

In conclusion, it has been shown that alloying with Ta improves the thermal stability of coatings within the $Ti_{1-x}Al_xN$ system by retarding the decomposition of the supersaturated solid solution into its stable constituents c-TiN and w-AlN. Therefore, the hardness of coatings after vacuum annealing up to 1000 °C increases with increasing Ta content. The high-temperature properties can be further improved by adjusting the bias voltage during the deposition process, resulting in decomposition at higher temperatures and consequently, in enhanced mechanical properties up to higher temperatures.

However, it still has to be confirmed that the positive effects of Ta on the thermal stability of coatings within the $Ti_{1-x}Al_xN$ system also enhance their tribological properties effectively. Furthermore, investigations concerning the hex-Ta_2N phase have to be carried out, to obtain a better understanding of its influence on the mechanical properties of the system.

Appendix

Within this section, the findings obtained on the thermal stability of the $Ti_{0.6}Al_{0.4}N$ coating are summarized. Figure A.1 presents the heat flow, which was recorded during DSC measurements of three powdered $Ti_{0.5}Al_{0.5}N$ coatings. The coatings were deposited at three different bias voltages, namely V_B = -40 V, V_B = -100 V and an increasing bias voltage from -40 V at the interface to -70 V at the surface of the coating (BG setting). A discussion of latter can be found in section 6.1.3. The first two exothermic peaks, observed at temperatures below 900 °C in Figure A.1, can be related to recovery processes and decomposition, respectively. Both peaks are less pronounced for the coating deposited at the low bias voltage compared to the coatings synthesized at the high bias voltage or at the bias gradient. The third exothermic peak can be detected between 1100 and 1300 °C and is related to the formation of w-AlN, which starts at the lowest temperature for the coating synthesized at V_B = -100 V. Deposition at a low bias voltage results in a retarded formation of w-AlN due to a larger grain size in the coatings and consequently, less nucleation sites.

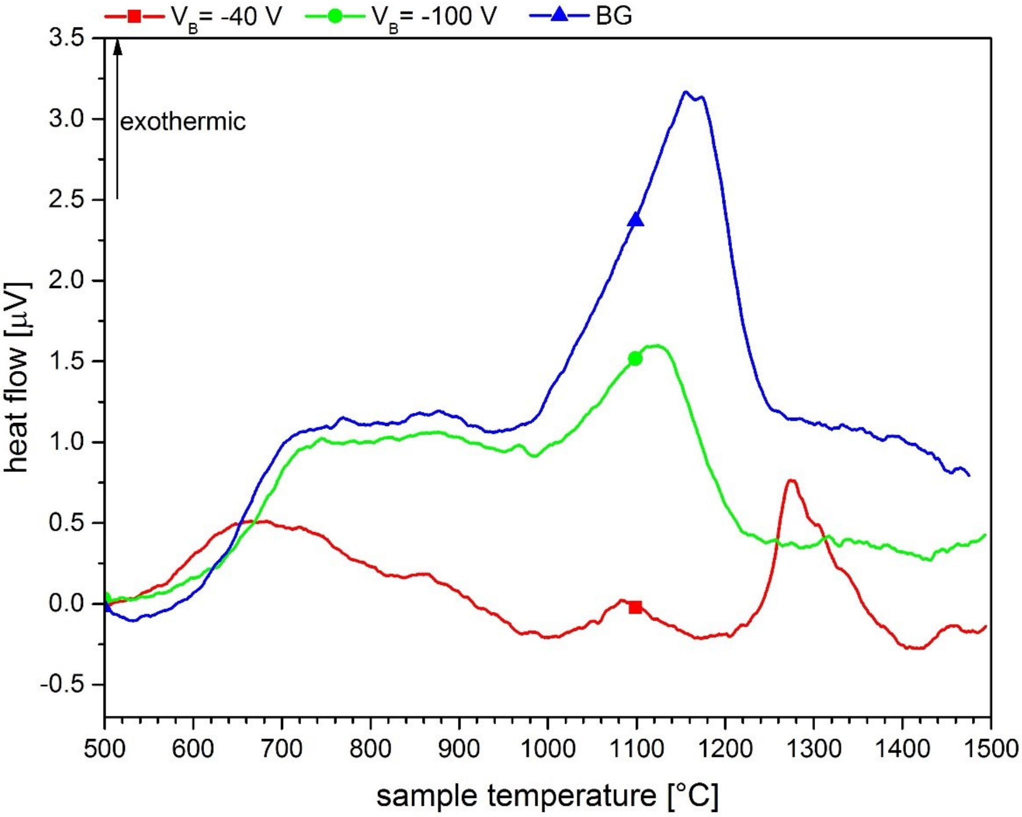

Figure A.1: Heat flow recorded during qualitative DSC measurements of three powders prepared from $Ti_{0.5}Al_{0.5}N$ coatings, which were synthesized at bias voltages V_B of -40 V, -100 V and a bias gradient (BG).

Three heat flow curves recorded during DSC measurements of $Ti_{0.475}Al_{0.475}Ta_{0.05}N$ coatings grown at different bias voltages are shown in Figure A.2. The discussion of the coating deposited with the BG parameter set can be found in section 6.1.3. Recovery and decomposition can be attributed to the exothermic peaks measured at temperatures below 1000 °C. They are most pronounced for the coating synthesized applying a bias gradient and weakest for the system deposited at V_B = -40 V. The exothermic peak at temperatures higher than 1100 °C is attributed to the formation of w-AlN, which is most distinct for the coating grown using a bias gradient. However, its maximum is shifted to lower temperatures for V_B = -100 V and to higher temperatures for V_B = -40 V.

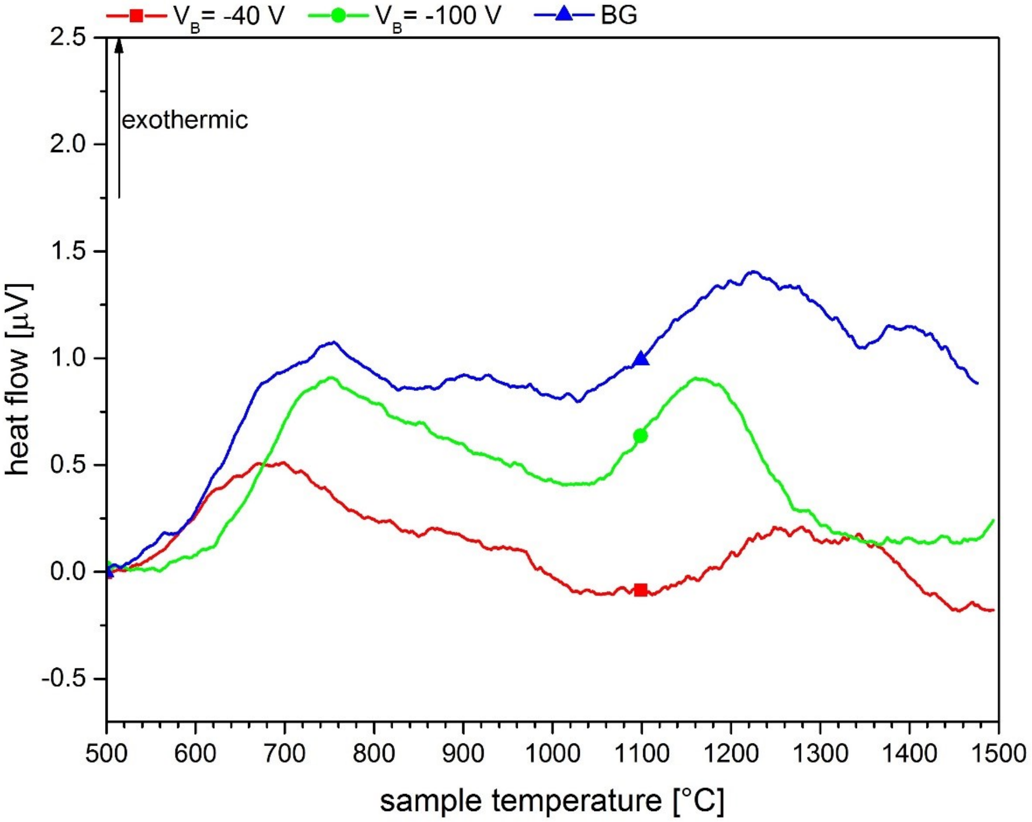

Figure A.2: Heat flow recorded during qualitative DSC measurements of three powders prepared from $Ti_{0.475}Al_{0.475}Ta_{0.05}N$ coatings, which were synthesized at bias voltages V_B of -40 V, -100 V and a bias gradient (BG).

Figure A.3 shows the heat flow in dependence of the sample temperature recorded during DSC measurements of three $Ti_{0.6}Al_{0.4}N$ coatings. The coatings were synthesized applying three different bias voltages. For all three systems, recovery and decomposition can be attributed to the first two exothermic peaks. A low bias voltage results in an early onset of recovery and an overall lower heat flow, compared to higher bias voltages. Additionally, the third peak is shifted to higher temperatures. The coating deposited using a bias gradient shows the highest energy loss when heating up to 1000 °C. Similar results were obtained for the $Ti_{0.5}Al_{0.5}N$ system synthesized with the same parameter set. Due to the bias gradient, the lattice parameter changes during the deposition process and consequently, strong recovery of microstrain can also be expected for the $Ti_{0.6}Al_{0.4}N$ system.

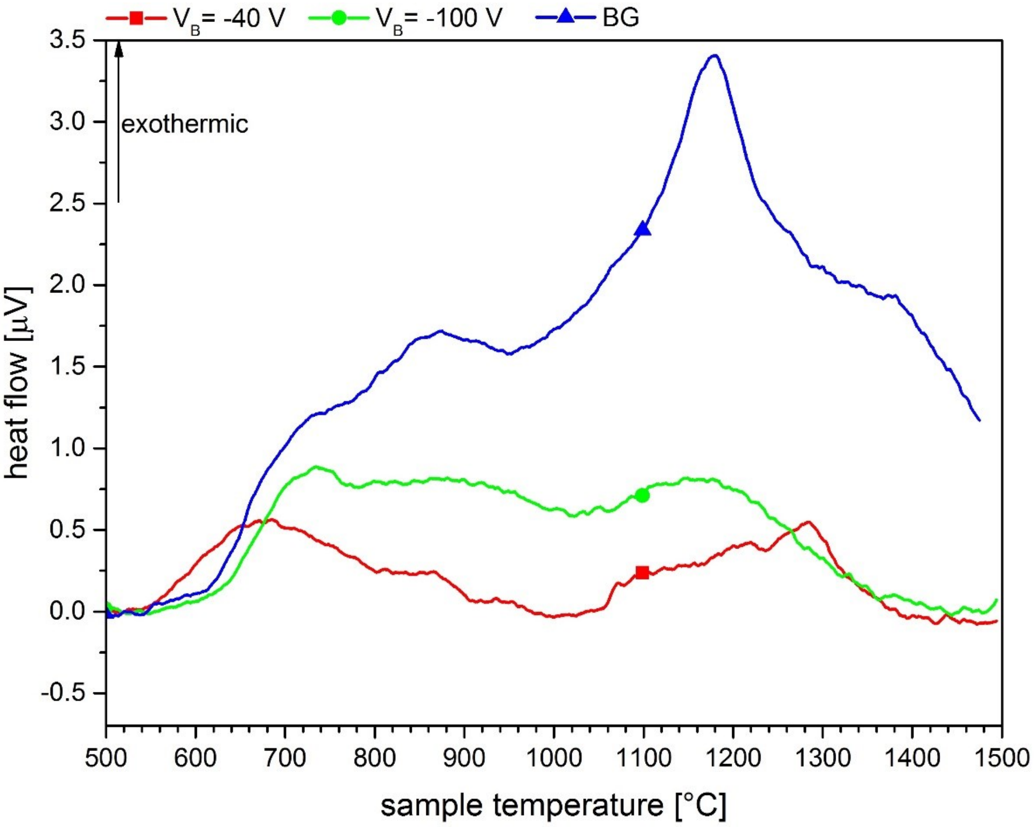

Figure A.3: Heat flow recorded during qualitative DSC measurements of three powders prepared from $Ti_{0.6}Al_{0.4}N$ coatings, which were synthesized at bias voltages V_B of -40 V, -100 V and a bias gradient (BG).

X-ray diffractograms of three $Ti_{0.6}Al_{0.4}N$ coatings, which where synthesized on cemented carbide substrates applying different bias voltages, are shown in Figure A.4. The coatings were annealed at temperatures between 700 and 1000 °C to investigate the evolution of the microstructure. Figure A.4a shows the diffractograms of the coating deposited at V_B = -40 V. The peak shift towards higher angles after annealing at 700 °C can be attributed to recovery, while decomposition starts after annealing at 750 °C, with c-TiN rich domains forming first. w-AlN can be detected after annealing at 950 °C. The diffractograms of coatings synthesized at V_B = -100 V are summarized in Figure A.4b and display broader (200) peaks with a lower intensity compared to the coating grown at the lower bias voltage. A pronounced peak shift towards higher diffraction angles can be detected after annealing at 700 °C, indicating more distinct recovery processes than in the coating deposited at V_B = -40 V. Decomposition can be detected after annealing at 800 °C, with shoulders forming on the c-TiN side of the $T_{1-x}Al_xN$ peaks. Formation of w-AlN starts after annealing at 950 °C. Compared to the coating shown in Figure A.4a, more w-AlN is formed. The diffractograms of the coating synthesized applying a bias gradient are presented in Figure A.4c and display (200) peaks with a high intensity and width. The shape and intensity of the peaks are comparable to those of the coating deposited at V_B = -40 V and V_B = -100 V, respectively. After annealing at 700 °C, a peak shift towards higher angles is detected, indicating recovery processes. The $Ti_{0.6}Al_{0.4}N$ matrix starts to decompose after annealing at 800 °C and w-AlN forms at annealing temperatures higher than 900 °C.

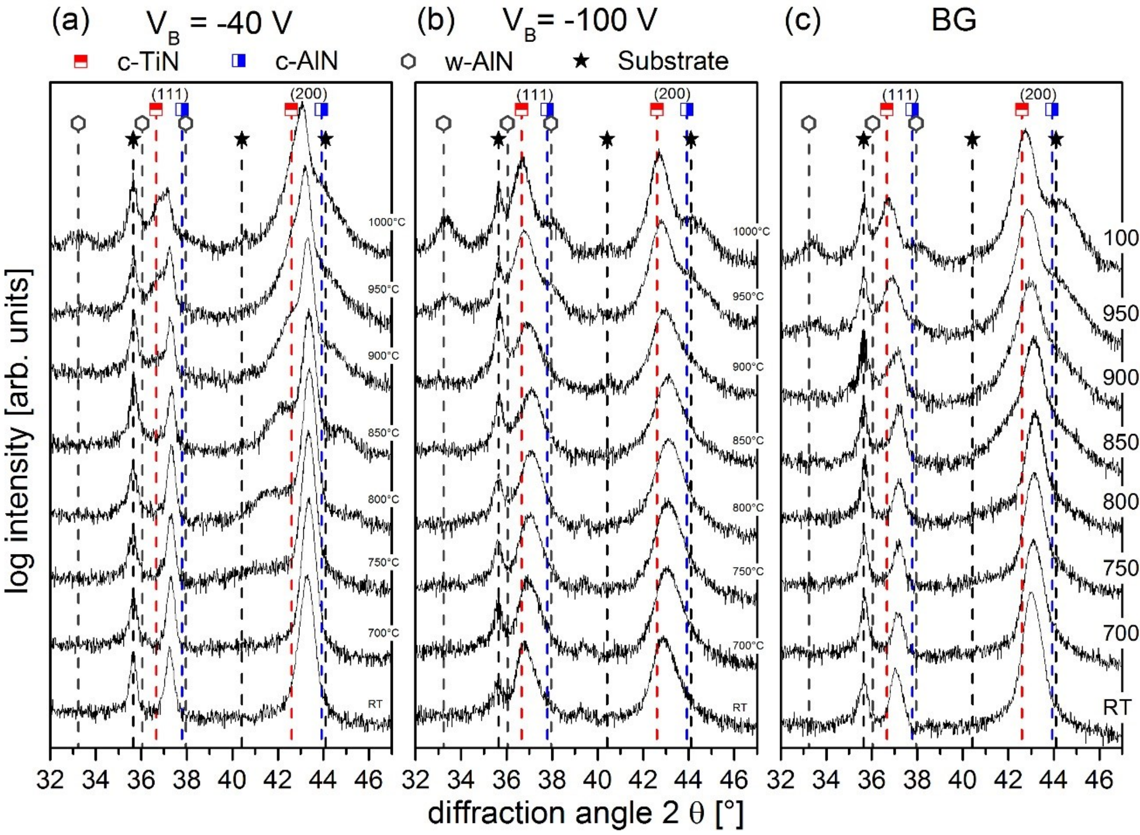

Figure A.4: Grazing incidence X-ray diffractograms for $Ti_{0.6}Al_{0.4}N$ coatings deposited with the bias voltage (V_B) sets (a) V_B = -40 V, (b) V_B = -100 V and (c) BG (= bias gradient) on cemented carbide substrates before annealing (RT) and after annealing in a vacuum furnace.

Figure A.5 shows the hardness of three $Ti_{0.6}Al_{0.4}N$ coatings, deposited on cemented carbide substrates at three different bias voltages, after annealing in a vacuum furnace. For the coating deposited at V_B = -40 V and V_B = -100 V, hardness values of ~ 26 GPa and ~34 GPa were obtained in the as-deposited state, respectively. The coating grown while changing the bias voltage between -40 V at the interface to -70 V at the surface has a hardness of ~ 30.5 GPa in the as-deposited state. Typically smaller grain sizes and higher compressive stresses are observed for coatings grown at higher bias voltages [16, 49], which also explains the higher hardness values. The $Ti_{0.6}Al_{0.4}N$ coating synthesized at -40 V shows a hardness maximum of ~ 28 GPa after annealing at 750 °C. For annealing temperatures between 800 and 900 °C, the hardness remains constant at ~ 26 GPa and decreases for higher annealing temperatures, reaching a minimum value of ~ 22.5 GPa after annealing at 1000 °C. The hardness of the coating grown at V_B = -100 V remains at ~ 34 GPa up to annealing temperatures of 700 °C. After annealing between 800 and 900 °C, a hardness of ~ 31 GPa is observed and it decreases to ~ 27 GPa for an annealing temperature of 1000 °C. Compared to the coating deposited at a lower bias voltage, the hardness is ~ 5 GPa higher for annealing temperatures higher than 750 °C. The coating grown with a bias gradient exhibits a hardness of ~ 30.5 GPa up to annealing temperatures of 950 °C. For even higher annealing temperatures, the hardness decreases to 27 GPa. The hardness values up to annealing temperatures of 750 °C lie between those of the coatings deposited at constant bias voltages, and they are similar to the coating deposited at V_B = -100 V for higher annealing temperatures.

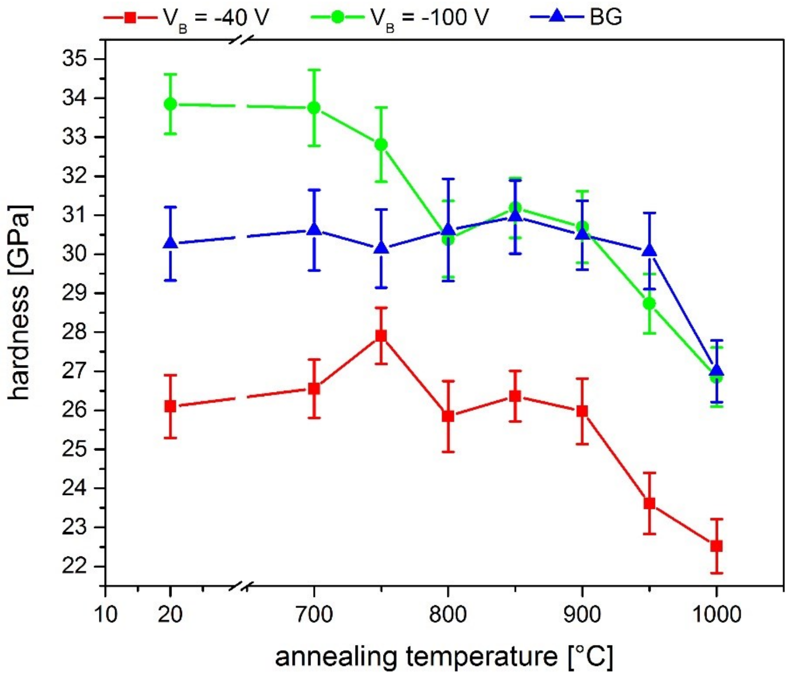

Figure A.5: Hardness evolution as a function of vacuum annealing treatments of $Ti_{0.6}Al_{0.4}N$ coatings grown using different bias voltages (V_B) on cemented carbide substrates (BG = bias gradient).

References

[1] R. F. Bunshah (Ed.), *Handbook of Hard Coatings: Deposition Technologies, Properties and Applications*, Noyes Publications, Park Ridge, N.J, Norwich, N.Y 2001.

[2] S. Paldey, S. Deevi, Single layer and multilayer wear resistant coatings of (Ti,Al)N: a review. *Mat. Sci. Eng. A* 2003, *342 (1–2)*, 58.

[3] I. Suni, Thermal oxidation of reactively sputtered titanium nitride and hafnium nitride films. *J. Electrochem. Soc.* 1983, *130 (5)*, 1210.

[4] M. Wittmer, Oxidation kinetics of TiN thin films. *J. Appl. Phys.* 1981, *52 (11)*, 6659.

[5] O. Knotek, On structure and properties of sputtered Ti and Al based hard compound films. *J. Vac. Sci. Technol. A* 1986, *4 (6)*, 2695.

[6] W.-D. Münz, Titanium aluminum nitride films: A new alternative to TiN coatings. *J. Vac. Sci. Technol. A* 1986, *4 (6)*, 2717.

[7] A. Kimura, H. Hasegawa, K. Yamada, Effects of Al content on hardness, lattice parameter and microstructure of $Ti_{1-x}Al_xN$ films. *Surf. Coat. Technol.* 1999, *120-121*, 438.

[8] M. Kathrein, C. Michotte, M. Penoy, Multifunctional multi-component PVD coatings for cutting tools. *Surf. Coat. Technol.* 2005, *200 (5-6)*, 1867.

[9] D. Holec, L. Zhou, R. Rachbauer, Alloying-related trends from first principles: An application to the Ti–Al–X–N system. *J. Appl. Phys.* 2013, *113 (11)*, 113510.

[10] R. A. Haefer (Ed.), *Oberflächen- und Dünnschicht-Technologie: Teil I: Beschichtungen von Oberflächen*, Springer, Berlin, Heidelberg 1987.

[11] R. F. Bunshah, *Deposition Technologies for Films and Coatings: Developments and Applications*, Noyes Publ, Park Ridge, NJ 1982.

[12] D. M. Mattox, *Handbook of Physical Vapor Deposition (PVD) Processing,* 2nd edn., William Andrew, Amsterdam 2010.

[13] A. Anders, *Cathodic Arcs: From Fractal Spots to Energetic Condensation*, Springer-Verlag New York, New York, NY 2008.

[14] M. Ohring, *Materials Science of Thin Films: Deposition and Structure,* 2nd edn., Academic Press, San Diego, Calif. 2002.

[15] J. Greene (Ed.), *Handbook of Crystal Growth*, Elsevier Science Publishers, Amsterdam 1993.

[16] A. Anders, A structure zone diagram including plasma-based deposition and ion etching. *Thin Solid Films* 2010, *518 (15)*, 4087.

[17] A. Movchan, A. V. Demchishin, Study of the structure and properties of thick vacuum condensates of nickel, titanium, tungsten, aluminia and zirconium dioxide. *Mat. Sci. Eng. A* 1969, *28 (83)*, 653.

[18] J. A. Thornton, Influence of apparatus geometra and deposition conditions on the structure and topography of thick sputtered coatings. *J. Vac. Sci. Technol.* 1974, *11 (4)*, 666.

[19] G. Gottstein, *Physikalische Grundlagen der Materialkunde*, Springer, Berlin, Heidelberg 1998.

[20] W. Schatt, H. Blumenauer (Eds.), *Werkstoffwissenschaft: 42 Tabellen,* 8th edn., Dt. Verl. für Grundstoffindustrie, Stuttgart 1996.

[21] R. Rachbauer, *Comparative Microstructural Investigationsof Ti-Al-N Thin Films Alloyed with Y or Nb, Diploma Thesis*, Leoben 2008.

[22] D. A. Porter, K. E. Easterling, M. Y. Sherif, *Phase Transformations in Metals and Alloys,* 3rd edn., CRC Press, Hoboken 2009.

[23] R. Rachbauer, *Age Hardening in Transition Metal Aluminium Nitride Thin Films Studies at the Atomic Scale, PhD Thesis*, Leoben 2011.

[24] H. Holleck, Metastable coatings — Prediction of composition and structure. *Surf. Coat. Technol.* 1988, *36 (1-2)*, 151.

[25] R. Cremer, M. Witthaut, D. Neuschütz, in *Werkstoffwissenschaft: 42 Tabellen* (Eds.: W. Schatt, H. Blumenauer), Dt. Verl. für Grundstoffindustrie, Stuttgart 1996, 249.

[26] M. Pfeiler, *Synthesis-Structure-Property Relations of TiAlN based Hard Coatings, PhD Thesis*, Leoben 2008.

[27] P. H. Mayrhofer, A. Hörling, L. Karlsson, Self-organized nanostructures in the Ti–Al–N system. *Appl. Phys. Lett.* 2003, *83 (10)*, 2049.

[28] R. Rachbauer, D. Holec, P. H. Mayrhofer, Increased thermal stability of Ti–Al–N thin films by Ta alloying. *Surf. Coat. Technol.* 2012, *211*, 98.

[29] F. Vaz, L. Rebouta, M. Andritschky, Thermal oxidation of $Ti_{1-x}Al_xN$ coatings in air. *J. Eur. Ceram. Soc.* 1997, *17 (15-16)*, 1971.

[30] L. Chen, J. Paulitsch, Y. Du, Thermal stability and oxidation resistance of Ti-Al-N coatings. *Surf. Coat. Technol.* 2012, *206-318 (11-12)*, 2954.

[31] A. Hörling, L. Hultman, M. Odén, Thermal stability of arc evaporated high aluminum-content $Ti_{1-x}Al_xN$ thin films. *J. Vac. Sci. Technol.* 2002, *20 (5)*, 1815.

[32] K. Resch, P. H. Mayrhofer, Temperature driven evolution of thermal, electrical, and optical properties of Ti–Al–N coatings. *Acta Mater.* 2012, *60 (5)*, 2091.

[33] A. Hörling, L. Hultman, M. Odén, Mechanical properties and machining performance of $Ti_{1-x}Al_xN$-coated cutting tools. *Phys. Rev. B* 2005, *191 (2-3)*, 384.

[34] R. Rachbauer, D. Holec, P. H. Mayrhofer, Phase stability and decomposition products of Ti–Al–Ta–N thin films. *Appl. Phys. Lett.* 2010, *97 (15)*, 151901.

[35] R. Hollerweger, H. Riedl, J. Paulitsch, Origin of high temperature oxidation resistance of Ti–Al–Ta–N coatings. *Surf. Coat. Technol.* 2014, *257*, 78.

[36] M. Pfeiler, C. Scheu, H. Hutter, On the effect of Ta on improved oxidation resistance of Ti–Al–Ta–N coatings. *J. Vac. Sci. Technol. A* 2009, *27 (3)*, 554.

[37] M. Pfeiler, G. A. Fontalvo, J. Wagner, Arc evaporation of Ti–Al–Ta–N coatings: The effect of bias voltage and Ta on high-temperature tribological properties. *Tribol. Lett.* 2008, *30 (2)*, 91.

[38] M. E. Brown (Ed.), *Handbook of Thermal Analysis and Calorimetry: Principles and Practice*, ELSEVIER SCIENCE B.V., Amsterdam 1998.

[39] B. D. Cullity, S. R. Stock, *Elements of X-Ray Diffraction,* 3rd edn., Pearson/Prentice Hall, Upper Saddle River, NJ 2001.

[40] International Center for Diffraction Data, PDF-2/Release 2007, Card Number 00-038-1420, 2007.

[41] International Center for Diffraction Data, PDF-2/Release 2007, Card Number 00-038-1495, 2007.

[42] L. Vegard, Die Konstitution der Mischkristalle und die Raumfüllung der Atome. *Z. Phys.* 1921, *5*, 17.

[43] J. H. Hubbell, S. M. Seltzer, *Tables of X-ray mass attenuation coefficients and mass energy-absorption coefficients from 1 keV to 20 MeV for elements Z = 1 to 92 and 48 additional substances of dosimetric interest*. http://physics.nist.gov/PhysRefData/XrayMassCoef/tab3.html, January 13, 2016.

[44] C. Stampfl, A. J. Freeman, Stable and metastable structures of the multiphase tantalum nitride system. *Phys. Rev. B* 2005, *71 (2)*.

[45] C. M. Koller, R. Hollerweger, C. Sabitzer, Thermal stability and oxidation resistance of arc evaporated TiAlN, TaAlN, TiAlTaN, and TiAlN/TaAlN coatings. *Surf. Coat. Technol.* 2014, *259*, 599.

[46] C. M. Koller, A. Kirnbauer, R. Rachbauer, Thermally-induced phase transformation sequence of arc evaporated Ta–Al–N coatings. *Scripta Mater.* 2016, *113*, 75.

[47] T. Chihi, J. C. Parlebas, M. Guemmaz, First principles study of structural, elastic, electronic and optical properties of Nb_2N and Ta_2N compounds. *Phys. Stat. Sol. B* 2011, *248 (12)*, 2787.

[48] C. Wüstefeld, D. Rafaja, V. Klemm, Effect of the aluminium content and the bias voltage on the microstructure formation in $Ti_{1-x}Al_xN$ protective coatings grown by cathodic arc evaporation. *Surf. Coat. Tech.* 2010, *205 (5)*, 1345.

[49] M. Ahlgren, H. Blomqvist, Influence of bias variation on residual stress and texture in TiAlN PVD coatings. *Surf. Coat. Technol.* 2005, *200 (1-4)*, 157.

[50] P. H. Mayrhofer, L. Hultman, J. M. Schneider, Spinodal decomposition of cubic $Ti_{1-x}Al_xN$: Comparison between experiments and modeling. *Int. J. Mat. Res.* 2007, *98 (11)*, 1054.

[51] I. Petrov, P. B. Barna, L. Hultman, Microstructural evolution during film growth. *J. Vac. Sci. Technol. A* 2003, *21 (5)*, S117.

[52] V. D. Ovcharenko, A. S. Kuprin, G. N. Tolmachova, Deposition of chromium nitride coatings using vacuum arc plasma in increased negative substrate bias voltage. *Vac.* 2015, *117*, 27.

[53] N. Schalk, C. Mitterer, J. Keckes, Influence of residual stresses and grain size on the spinodal decomposition of metastable $Ti_{1-x}Al_xN$ coatings. *Surf. Coat. Technol.* 2012, *209*, 190.